

Effect of non-uniform heating on scCO₂ heat transfer deterioration

Bingguo Zhu^a, Jinliang Xu^{a,b,*}, Haisong Zhang^a, Jian Xie^{a,b}, Mingjia Li^c

^a Beijing Key Laboratory of Multiphase Flow and Heat Transfer for Low Grade Energy Utilization, North China Electric Power University, Beijing 102206, China

^b Key Laboratory of Power Station Energy Transfer Conversion and System, Ministry of Education, North China Electric Power University, Beijing 102206, China

^c Key Laboratory of Thermo-Fluid Science and Engineering of Ministry of Education, Xi'an Jiaotong University, Xi'an, Shanxi 710049, China



HIGHLIGHTS

- Non-uniform and uniform heating scCO₂ heat transfer experiments are performed.
- Non-uniform heating displays strong circular angles dependent heat transfer characteristic.
- Similarity analysis deals with heat transfer deterioration at supercritical pressures.
- SBO_{cr} is 8.908×10^{-4} for non-uniform heating which is larger than uniform heating.
- The buoyancy effect has no connection with heat transfer deterioration.

ARTICLE INFO

Keywords:

ScCO₂ power cycle
Heat transfer deterioration
Critical heat flux
Pseudo-boiling
Non-uniform heating

ABSTRACT

The accurate prediction of heat transfer deterioration (HTD) is important to ensure the safe operation of scCO₂ cycles driven by various heat sources. Here, the scCO₂ heat transfer experiment is performed in a 10 mm diameter vertical tube, covering the ranges of pressures 7.51–21.1 MPa, mass fluxes 488–1500 kg/m²s and heat fluxes 43.7–488 kW/m². Both uniform heating and non-uniform heating cases are dealt with, but more attention is paid on non-uniform heating. We show that non-uniform heating displays strong circumference angles dependent heat transfer characteristic. Normal heat transfer (NHT) displays gentle rise of wall temperatures along flow length, but for HTD, wall temperature peak is detected ahead of pseudo-critical point. Pseudo-boiling is introduced to deal with scCO₂ heat transfer. Heat added to scCO₂ is decoupled into a temperature rise part and a phase change part. Flow structure includes a vapor-like fluid near tube wall and a liquid-like fluid in tube core. The analogy between subcritical boiling and supercritical heat transfer results in a supercritical-boiling-number SBO to govern the vapor layer thickness. Sudden change from NHT to HTD is found when crossing a critical SBO_{cr} , which is 5.126×10^{-4} for uniform heating based on our experimental data and other data in the literature, but becomes 8.908×10^{-4} for non-uniform heating using our experimental data. Compared to uniform heating, non-uniform heating is found to delay the occurrence of HTD. The criterion presented here is useful to avoid the occurrence of HTD in the design and operation of scCO₂ cycles.

1. Introduction

Supercritical fluids have wide applications in engineering systems. A recent review by Pizzarelli shows that the supercritical fluid can be used as the coolant in Supercritical Water-Cooled Reactors (SCWR), oxygen-methane rocket engines, supercritical CO₂ power cycles, trans-critical CO₂ heat pumps and supercritical water oxidation [1]. As a promising type of nuclear reactor, SCWR is expected to be available after 2030. Thanks to the elimination of steam separator and dryer, SCWR enables significant system simplification. Due to increased inlet

turbine temperature, a SCWR will achieve efficiencies of about 44%, compared to ~34% for current Light-Water-Reactors.

Heat transfer deterioration (HTD) is important for design and operation of supercritical fluid systems. HTD refers to wall temperature peak of the heater, which may lead to the heater failure due to burn-out. To avoid the occurrence of HTD, sufficient experiment data should be obtained, and reliable prediction criterion should be developed. Great attention has been paid on HTD (see Table 1). We examine the HTD studies for supercritical water first. The available experimental studies majorly focus on the uniform heating applied to circular tubes.

* Corresponding author at: Beijing Key Laboratory of Multiphase Flow and Heat Transfer for Low Grade Energy Utilization, North China Electric Power University, Beijing 102206, China.

E-mail address: xjl@ncepu.edu.cn (J. Xu).

<https://doi.org/10.1016/j.applthermaleng.2020.115967>

Received 14 April 2020; Received in revised form 3 July 2020; Accepted 24 August 2020

Available online 30 August 2020

1359-4311/ © 2020 Elsevier Ltd. All rights reserved.

Nomenclature

a	coefficients
b	heat produced by control volume per unit length, W/m
Bo	boiling number, 1
Bu	Buoyancy parameters, 1
Bu^*	Buoyancy parameters, 1
C_0-C_4	coefficients
c	critical point
c_p	specific heat, J/kg \cdot °C
D	bubble diameter, m
d	tube diameter, m
e	east
F	force, N
g	gravitational acceleration, m/s 2
G	mass flux, kg/m 2 s
Gr	Grashof number, 1
h	heat transfer coefficients, W/m 2 K
i	enthalpy, J/kg
K	non-dimensional number, 1
k	coefficients
L	length, m
M_s	the radial direction grid number in the silver domain
M_t	the radial direction grid number in the whole computation domain
m	flow rate, kg/s
n	north
P	pressure, Pa
p	peak
Pr	Prandtl number, 1
Q	heat created by electrical resistance, W
q	heat flux, W/m 2
R	electrical resistance per unit length, Ω /m
Re	Reynolds number, 1
r	radius, m
S	heat source, W/m 3
s	south
T	temperature, °C
T^+	the ending temperature of pseudo-boiling, °C
T^-	the starting temperature of pseudo-boiling, °C
t	time
u	velocity, m/s
V	voltage across per unit length, V
w	west

Greek symbols

ε	constant
λ	heat conductivity coefficient, W/m \cdot °C
φ	circular angle
δ	thickness, m
θ	angle
ρ_e	specific resistance, Ω m
ρ	density, kg/m 3
π	pi
β	thermal expansion coefficient, 1/K
μ	viscosity coefficient, Pa \cdot s
Δr_s	distance between two nodes in the silver domain
Δr_t	distance between two nodes in the tube domain
Δr	radial distance difference

ΔS	cross-section area of the grid
ΔT	temperature overshoot
Δt	time change
ΔV	volume change, m 3
Δi	pseudo-boiling enthalpy, J/kg
$\Delta \theta$	circumferential angle difference
ν	kinematic viscosity, m 2 /s

Subscripts

ave	average
b	bulk
CHF	critical heat flux
cr	critical
c	cold region
D-B	Dittus-Boelter correlation
E	east
f	liquid phase
fg	saturated CO $_2$ turns into saturated vapor
g	gas phase
ho	hole
h	hot region
in	inlet
I'	inertia
i	inner
l	left
M'	momentum
n	non-uniform
N	north
o	outer
out	outlet
pc	pseudo critical
pt	latent heat
r	right
S	south
sen	sensible heat
t	total
u	uniform
W	west
WL	Widom line
w	inner wall
z	axial location

Acronyms

CFD	computational fluid dynamics
CSR	cold-side region
CHF	critical heat flux
DC	direct-current
exp.	experimental study
HTD	heat transfer deterioration
HSR	hot-side region
NUH	non-uniform heating
NHT	normal heat transfer
SBO	supercritical-boiling-number
SCWR	supercritical Water-Cooled Reactors
SHT	supercritical heat transfer
TDMA	the tridiagonal matrix algorithm
UH	uniform heating
V	valve

Heat flux at HTD condition is defined as the critical heat flux $q_{w,CHF}$. The simple treatment is to plot $q_{w,CHF} \sim G$ curve to distinguish NHT and HTD, where G is the mass flux. Different correlations are reported in the

literature such as $q_{w,CHF} = 0.453G$ [11], $q_{w,CHF} = -58.97 + 0.745G$ [14] and $q_{w,CHF} = 0.2G^{1.2}$ [22]. These correlations are suitable for their own experimental data, but difficult to be extended for users. It is

Table 1
A review of supercritical heat transfer.

NO.	Ref. working fluid and method	P (MPa) P/P_{cr}	G (kg/m ² s)	q _w (kW/m ²)	d _i (mm)	HTD mechanism	judgment of HTD and prediction
1	[2], H ₂ O/UH/exp.	22.5–30/ 1.018–1.358	376–1500	148–1410	3–38	/	The occurrence of peak wall temperature is defined as HTD. $q_{CHF} = 0.457 \cdot G^{1.09} \left(1 - 0.035 \left(\frac{d_i}{30} \right)^{1.96} \left(\frac{P}{32.1} \right)^{7.16} \right)$ The occurrence of peak wall temperature is defined as HTD.
2	[3], H ₂ O/UH/CFD	25/1.131	$Re_{in} = 5400$	100	/	The large property variations near wall impair heat transfer. The flow acceleration induced by thermal expansion shows an obvious suppression on turbulence but does not affect heat transfer.	
3	[4], H ₂ O/UH/exp.	22.5–31/ 1.018–1.403	203–3000	166–2960	0.7–38.1	/	HTD occurs if $h_{exp}/h_{D-B} < 0.3$. $q_{CHF} = 825.2 \cdot G^{0.8325} \cdot d_i^{-0.4958} \cdot P^{-0.7486} \cdot T_{in}^{-0.8125}$
4	[5], H ₂ O and CO ₂ /UH/exp.	Water: 22.5–31/ 1.018–1.403 CO ₂ : 7.44–9.22/ 1.009–1.250	Water: 201–1500 CO ₂ : 230–3055	Water: 88–1741 CO ₂ : 6.8–929	Water: 4–22 CO ₂ : 4–22	The buoyancy force and flow acceleration even the velocity profile, decrease the shear stress and weaken the turbulence.	Criterion 1: HTD occurs with peak wall temperatures; criterion 2: HTD occurs when $h_{exp}/h_{D-B} < 0.3$ or $h_{exp}/h_{D-B} < 0.5$ or $h < 8 \text{ kW/m}^2\text{K}$, $T_w > 580 \text{ }^\circ\text{C}$; criterion 3: T_w rises sharply beyond the pseudo-critical point.
5	[6], H ₂ O/UH/exp.	25–28/ 1.131–1.267	400–800	400–1000	/	HTD occurs due to buoyancy and flow acceleration effect.	T_w has a sharp rise near the pseudo-critical point.
6	[7], H ₂ O/UH/exp.	23–26/ 1.041–1.177	432–1775	189–1498	7.6, 10, 15.3	/	Peak T_w occurs ahead of pseudo-critical point, or T_w sharply rises beyond pseudo-critical point.
7	[8], H ₂ O/UH/NUH/exp/CFD	24–32/ 1.086–1.448	400–690	160–340	19	The integral of specific heat in the buffer layer and the buoyancy effect affect heat transfer.	HTD is defined as having peak wall temperatures.
8	[9], H ₂ O/UH/exp./CFD	23–25/ 1.041–1.131	450–1200	400–1000	/	HTD is caused by the decreased velocity gradient and shear stress, and the suppression of the turbulence.	HTD is identified if $h_{exp}/h_{D-B} < 1$.
9	[10], H ₂ O/UH/exp.	22.5–31.03/ 1.018–1.404	203–2149	150–1650	7.6–38.1	/	HTD occurs if $h_{exp}/h_{D-B} < 0.3$. $q_{CHF} = 0.000255 \cdot G^{0.823} \cdot (30 - d_i)^{0.296} \cdot \left(\frac{c_{p,pc}}{\beta_{pc}} \right)^{0.912}$
10	[11], H ₂ O/NUH/CFD	24.5/1.109	800–1800	300–800	7.5	HTD is caused by the buoyancy force and flow acceleration.	HTD occurs if $h_{exp}/h_{D-B} < 0.45$. $q_{CHF} = 0.453 \cdot G$
11	[12], H ₂ O/NUH/CFD	24.82/1.123	404	158–370	18.5	Turbulent quantities in HTD region, similar to the wall region for isothermal flow, play an important role in heat transfer.	/
12	[13], H ₂ O/UH/exp./CFD	23–25/ 1.041–1.13	596, 2021	772, 1385	10	Buoyancy effect causes shear stress and radial flow velocity redistribution, causing HTD.	/
13	[14], H ₂ O/UH/exp.	24/1.086	200–1500	70–1250	10	/	HTD is identified with observed peak wall temperatures. $q_{CHF} = -58.94 + 0.745 \cdot G$
14	[15], H ₂ O/UH/exp.	22.5–25/ 1.018–1.131	700–3500	300–2000	10, 20	/	HTD occurs if $h_{exp}/h_{D-B} < 0.3$. $q_{CHF} = 0.000135 \cdot G \cdot \left(\frac{c_{p,pc}}{\beta_{pc}} \right)$

(continued on next page)

Table 1 (continued)

NO.	Ref., working fluid and method	P (MPa) P/P _{cr}	G (kg/m ² s)	q _w (kW/m ²)	d _i (mm)	HTD mechanism	judgment of HTD and prediction
15	[16], CO ₂ /UH/CFD	8/1.084	200–1500	40–80	2, 6	Under heating condition, the buoyancy effect improves local heat transfer for downward flow while deteriorates that for upward flow.	/
16	[17], CO ₂ /UH/exp.	7.76–8.35/ 1.05–1.312	200–1500	3–450	4.6, 8, 22	Local thickening of viscous sublayer reduces heat diffusion. The decreasing Prandtl number induced by temperature rise weakens heat diffusion in viscous sublayer.	HTD is identified with peak wall temperatures. $q_{CHF} = 0.0002 \cdot G^2 (d_i = 4.6 \text{ mm})$; $q_{CHF} = 0.0002 \cdot G^2 (d_i = 8 \text{ mm})$; $q_{CHF} = 0.00015 \cdot G^2 (d_i = 22 \text{ mm})$ HTD occurs when $h_{exp}/h_{D, B} < 0.3$.
17	[18], CO ₂ /NUH/CFD	8.194–15/ 1.109–2.033	1000–2000	100–400	38		
18	[19], CO ₂ /UH/CFD	7.75–8.12/ 1.05–1.1	314–400	23–70	4.4–9	The effect of turbulent viscosity variations on HTD and the mechanisms are investigated.	/
19	[20], aviation kerosene/UH/exp./CFD	3–4/ 1.25–1.667	196–255	190–300	1.8	Effects of mass flow rate, heat flux, pressure and inlet temperature on HTD were studied.	Two types of HTD were observed.
20	[21], methane/UH/CFD	13/2.832	8500	1000–8000	4		$(q_w/G)_{CHF} = 43.2 \times 10^{-6} \cdot P + 31.4$

Note: exp. means experimental study, CFD means Computational fluid dynamics, UH means uniform heating, NUH means non-uniform heating.

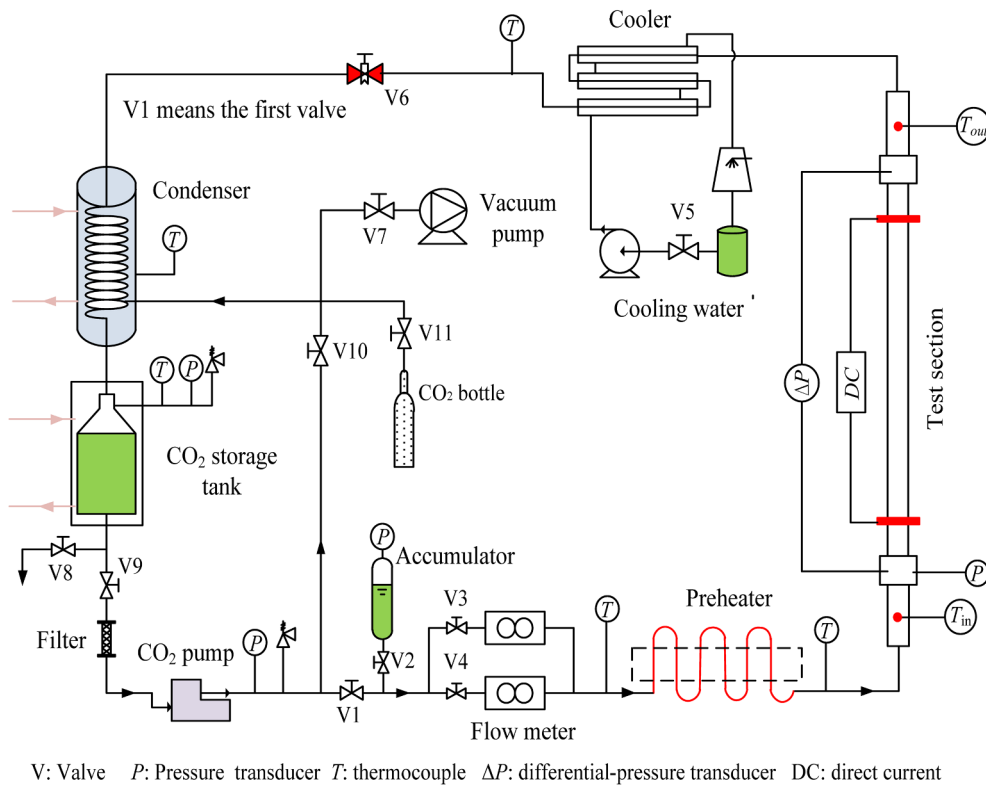


Fig. 1. Schematic diagram of experimental setup.

known that $q_{w,CHF}$ is influenced by physical properties, it is not acceptable that heat fluxes are correlated versus mass fluxes only.

Other investigators correlated critical heat fluxes dependent on more parameters expect G , such as Kong et al. [2], Ma et al. [4] and Schatte et al. [10], in which Ma et al. [4] gave the correlation as $q_{w,CHF} = C_0 G^{C_1} d_i^{C_2} P^{C_3} T_{in}^{C_4}$, where d_i , P and T_{in} are the inner tube diameter, pressure and inlet fluid temperature, respectively, C_0 – C_4 are the experiment determined coefficients (see Table 1). These correlations are purely mathematical treatment, and may not reflect the physical mechanism. The available references emphasize the importance of sharply varied physical properties and buoyancy/acceleration effects on supercritical heat transfer. Huang and Li [23] shows that the buoyancy effect is not properly addressed in the literature. Considerable disagreement is found between empirical correlations and experiment data. None of the buoyancy criteria can accurately predict the magnitude and onset of buoyancy force. Huang et al. [24] emphasizes the inconsistencies of supercritical heat transfer in the literature. Future works are recommended for supercritical heat transfer. Fewer studies are reported on the non-uniform heating for supercritical heat transfer including Zhang et al. [11] and Li et al. [12].

Another emerging field is the supercritical carbon dioxide (scCO₂) heat transfer. When the main vapor temperature is higher than 550 °C, the scCO₂ power cycle is believed to have higher efficiency than the water-steam Rankine cycle [25]. The compact system is another factor to attract engineers and industries. The scCO₂ cycles can be driven by various heat sources such as solar energy [26], nuclear energy [27] and coal [28]. In any scCO₂ power system, a heater is necessary to receive heat from a heat source to the cycle.

Most of the available studies on scCO₂ heat transfer cover narrow parameters range. Especially, experiments have been performed near the critical pressure of ~8 MPa [17,24,29,30]. For practical operation, the cycle pressure should be larger than 20 MPa [31]. There are no reliable predictions to calculate the occurrence of HTD. For solar driven scCO₂ cycle, a solar receiver receives sunlight heat with strong non-uniform heat fluxes over a tube cross section. For a scCO₂ coal fired

power plant, the tube side facing furnace flame has higher heat flux than the opposite tube side. The non-uniform heating causes deformed velocity profile over the tube cross-section. The uniform heating data cannot be directly used for non-uniform heating cases. Fan and Tang [18] numerically studied the scCO₂ heat transfer under non-uniform heating. They found that the circumferential thermal conduction in solid is important for scCO₂ heat transfer. To the authors' knowledge, the scCO₂ heat transfer experiment with non-uniform heating has not been reported.

Here, scCO₂ heat transfer is investigated emphasizing the non-uniform heating effect, covering wide ranges of $P = 7.51$ – 21.1 MPa, $G = 488$ – 1500 kg/m²s and $q_w = 43.7$ – 488 kW/m². Transition boundaries between NHT and HTD are paid more attention, in which both uniform heating and non-uniform heating cases are dealt with. We abandon the classical analysis of buoyancy effect, but introduce the heterogeneous scCO₂ structure instead. In textbooks, supercritical fluid has homogeneous structure containing single-phase only [32]. Recently, physicists experimentally identify the heterogeneous structure of supercritical fluids [33–35]. The molecular dynamics simulations show the vapor-like voids or cracks in supercritical fluid [36,37]. These findings inspire us to perform the analogy analysis between subcritical boiling and supercritical heat transfer. In the analysis, supercritical fluid is assumed to have a vapor-like fluid layer near tube wall and a liquid-like fluid in tube core. In such a way, the supercritical-boiling number SBO is theoretically deduced. Having this non-dimensional parameter, we show the sudden change from NHT to HTD when crossing a critical SBO .

2. Experimental apparatus and procedure

2.1. Experimental system

The experimental setup is shown in Fig. 1. The maximum CO₂ pressure reaches 25 MPa and the maximum CO₂ temperature attains 500 °C. The experiment loop includes a gas-vacuum/CO₂-charging

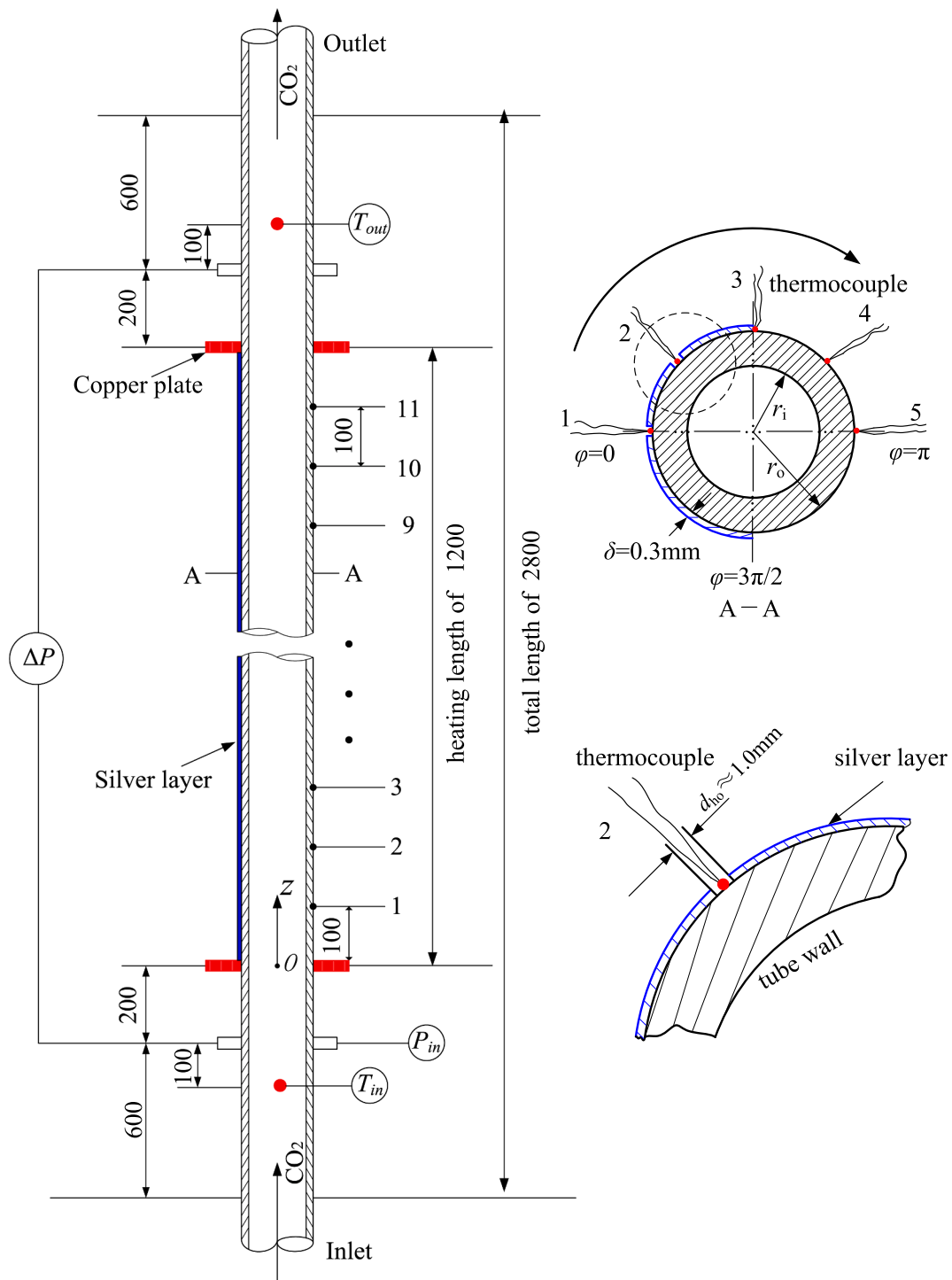


Fig. 2. Test section with non-uniform heating boundary condition.

system, a convective CO₂ loop, a cooling water loop, an electric heating system and a data acquisition system. Because non-condensable gas has apparent influence on heat transfer, the closed system is vacuumed to remove the non-condensable gas by switching on valve V7 and operating a vacuum pump. Then, CO₂ is charged into a storage tank from a high-pressure bottle by switching on valve V11 with valve V7 off. The outer surface of the CO₂ storage tank is cooled by the ~1 °C chiller water. The low temperature CO₂ liquid is sucked by a piston pump from a CO₂ storage tank. The total CO₂ flow is segmented into two streams, with one path being bypassed to the storage tank, and the other path consecutively flowing through two parallel mass flow meters, a

preheater and a test tube. The CO₂ vapor at the test tube outlet flows through a cooler and finally returns to a condenser. Heat received from the test tube is dissipated to cooling water. A cooling tower circulates the cooling water, dissipating heat to environment.

At the pump outlet, a pressure vessel stabilizer helps to achieve stable loop operation. The top volume of the pressure vessel is filled by high-pressure nitrogen gas. A flexible membrane separates the nitrogen gas from CO₂ liquid. The preheater and test tube are heated by low direct-current (DC) voltage by resistance heating. The heating power can be changed by varying the DC voltage. The preheater and test tube are heated by two independent power supply systems, having

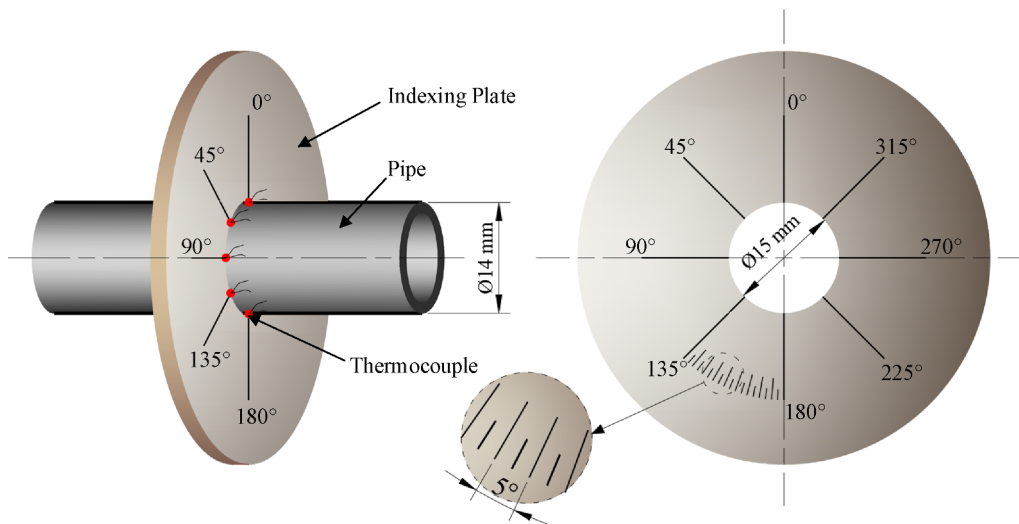


Fig. 3. Determination of thermocouples location along circumferential angles.

parameters of 54 kW (0–36 V, 0–1400 A), and 120 kW (0–40 V, 0–3000 A), respectively. The maximum heating power attains 120 kW, totally. The heating tube is electrically insulated from other part of the loop component.

2.2. Test tube

Two test tubes are used, one for uniform heating and the other for non-uniform heating. We describe the non-uniform heating tube first, which is vertically positioned and made of 1Cr18Ni9Ti. Due to higher carbon atoms concentration, 1Cr18Ni9Ti can sustain higher temperature than SUS316 and 304 at the same pressure. The tube has an outer diameter 14.0 mm and an inner diameter 10.0 mm (see Fig. 2). The tube is 2800 mm in length with an effective heating length of 1200 mm. Two stabilization sections, one ahead of the heating section and the other beyond the heating section, are arranged, each having a length of 800 mm. The DC power is applied via two copper electrodes, which are welded on the tube.

In a solar driven scCO_2 power generation system, the evacuated tube is a key element of parabolic trough solar collector, including an inner steel tube, an outer glass envelope, and an annular gap between them. ScCO_2 flows in the steel tube to extract sunlight energy. The sunny side of tube supplies higher heat flux but the night side has weak heat absorption. In a scCO_2 coal fired power plant, the cooling wall consists of parallel tubes. For each tube, the side facing combustion zone of furnace receives radiation heat flux, but the back side is thermally insulated. Both applications behave strong non-uniform heating characteristic.

A uniform silver layer is electroplated on a half-side of the tube to fulfill non-uniform heating (see cross-section A-A in Fig. 2). The silver layer thickness is $\sim 300 \mu\text{m}$. The silver layer and the tube can be considered as two parallel resistances, which are applied by a common voltage. Because silver has smaller electric resistance than tube, the silver layer dominates the heat generation. The test tube is wrapped by a ~ 50 mm thickness thermal insulation material to keep high thermal efficiency of the test tube.

Eleven cross-sections are arranged along flow direction (see Fig. 2). The distance between two neighboring cross-sections is 100 mm. On these cross-sections, thermocouple wires are directly welded on the tube surface to measure wall temperatures, thus the thermal conduction resistance between thermocouples and tube wall does not exist. The non-uniform heating induces obvious temperature difference along circumference direction, thus five thermocouples are arranged on each cross-section. Due to geometry symmetry on the plane of $\varphi = 0$ and

$\varphi = \pi$, the five thermocouples cover both the tube region with silver layer coating and the bare tube region. In order to precisely arrange thermocouples along the tube circumference angles, we fix each thermocouple location on outer tube wall on a processing platform. The tube is tightly held in a plate hole (see Fig. 3). The plate is precisely machined to mark the angle index, having an angle resolution of 5° . The angle uncertainty is estimated as 2.5° , which is 0.69% with respect to the whole angle range of 360° . Because thermocouple wires are difficult to be welded on silver layer, miniature holes (~ 1 mm diameter) are drilled to expose the local tube wall. Thus, thermocouples are directly welded on the tube wall. Totally, 55 thermocouples measure the outer wall temperatures.

For non-uniform heating, shorter tube is used to ensure uniform silver layer coating along tube length. Uniform heating is performed by applying voltage on the tube without coating silver layer, under which longer tube can be used. The uniform heating tube is identical to the non-uniform heating tube, except the longer effective heating length of 2000 mm. Totally 39 cross-sections are arranged for temperature measurements. The distance between two neighboring cross-sections is 50 mm. Because uniform heating creates wall temperatures independent on circumference angles, only one or two thermocouples are used on each cross-section. Due to different tube lengths used, comparative results between the two test tubes will be presented for wall temperatures versus bulk fluid enthalpies, not versus flow lengths.

2.3. Data reduction

It is necessary to determine the temperature fields in the solid material and the heat fluxes distribution on inner wall surface. For non-uniform heating, the silver layer has a thickness of $\sim 300 \mu\text{m}$, which is thinner than the tube wall. Different grid lengths in the radial direction are used in the silver layer domain and the tube wall domain. Thus, both the resistance heating of silver layer and tube wall can be considered. Due to the geometry symmetry against the center plane of $\varphi = 0$ and $\varphi = \pi$, only the half tube and the corresponding silver layer are considered. Specific points are marked in Fig. 4a and b. In the radial direction, M_s is the grid number in the silver domain, and M_t is the grid number in the whole computation domain. Here, $M_s = 5$ and $M_t = 25$ correspond to $\Delta r_s = 75 \mu\text{m}$ in the silver domain and $\Delta r_t = 100 \mu\text{m}$ in the tube domain.

Because the inner wall boundary condition is not known, the present problem belongs to an inverse heat conduction problem, which is solved by the *radial index forwarding method* [38]. Even though we lack the inner wall boundary condition, we have two boundary conditions

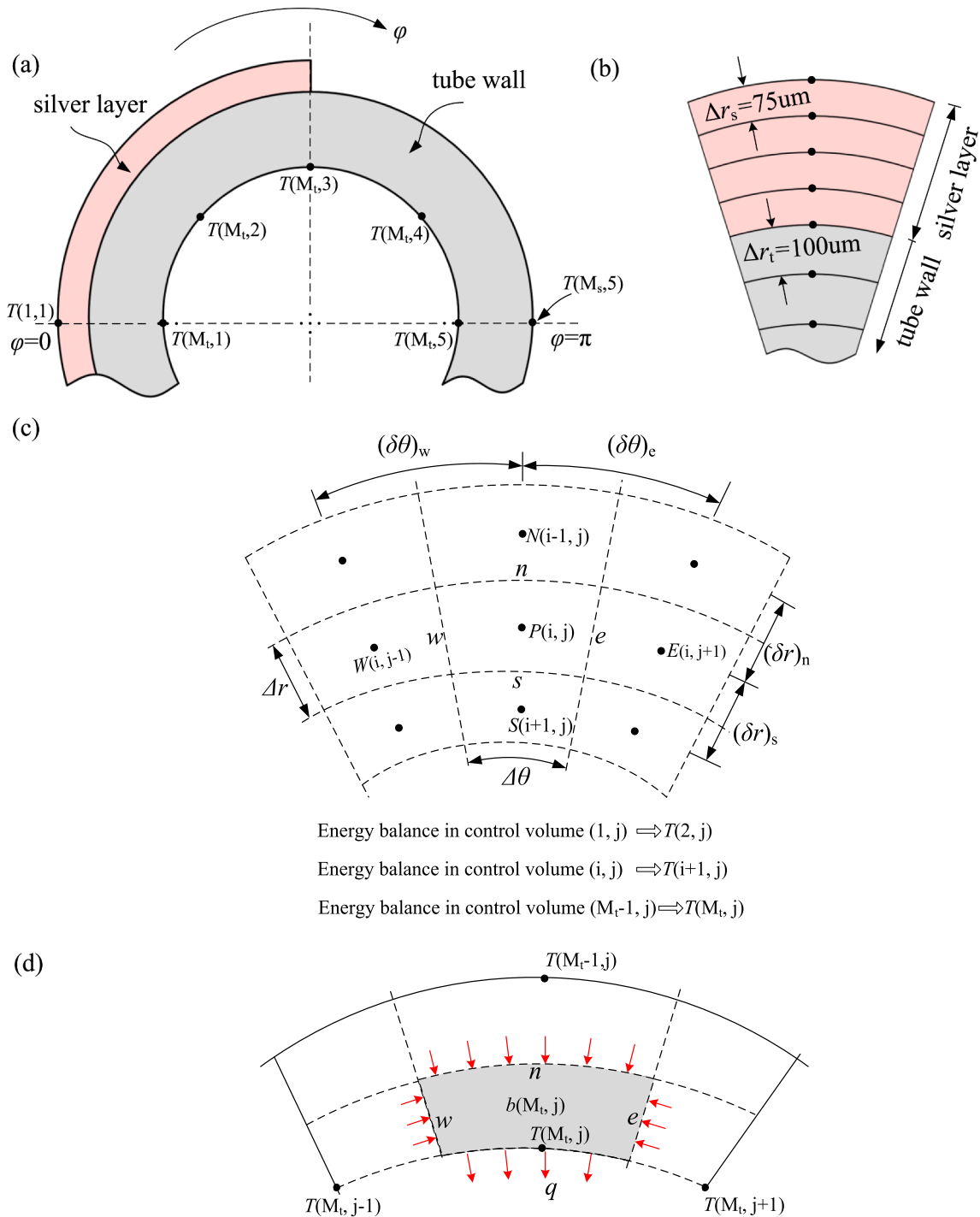


Fig. 4. Computation domain for the cross-section of tube wall and silver layer to determine temperatures and inner wall heat fluxes (a: geometry definition; b: different grid lengths in silver layer domain and tube wall domain; c: control volume for radial index forwarding method; d: energy balance in the grid close to the inner wall).

on the outer surface: the known outer wall temperatures measured by thermocouples, and the heat insulation boundary condition. Usually, the energy balance equation in a control volume (i, j) calculates the temperature $T(i, j)$. Different from the classical treatment, the radial index forwarding method calculates the temperature $T(i + 1, j)$ based on the control volume (i, j). The energy balance analysis in control volume (M_t - 1, j) yields the $T(M_t, j)$ expression. Hence, the number of equations is identical to the unknown variables.

The steady state, two-dimensional heat conduction problem with internal heat source is described by [38]

$$\frac{1}{r} \frac{\partial}{\partial r} \left(r \lambda \frac{\partial T}{\partial r} \right) + \frac{1}{r} \frac{\partial}{\partial \varphi} \left(\frac{\lambda}{r} \frac{\partial T}{\partial \varphi} \right) + S = 0 \quad (1)$$

where r is the radius, λ is the thermal conductivity of material, T is the temperature, φ is the circular angle and S is the internal heat source. Because heat source is generated by resistance heating, S is not zero.

For uniform heating, heat source is caused by the resistance heating of tube wall. However, for non-uniform heating, heat source is generated by both the silver layer and the tube wall. Referring to Fig. 4c, Eq. (1) has the following solution:

$$a_P T_P = a_W T_W + a_E T_E + a_N T_N + a_S T_S + b(i, j) \quad (2)$$

where $b(i, j)$ is heat generation rate in the control volume (i, j) . The coefficients are

$$\left. \begin{aligned} a_W &= \frac{\Delta r}{r_W (\delta_\theta)_W / \lambda_W} \\ a_E &= \frac{\Delta r}{r_e (\delta_\theta)_e / \lambda_E} \\ a_N &= \frac{r_n \Delta \theta}{(\delta_r)_n / \lambda_N} \\ a_S &= \frac{r_s \Delta \theta}{(\delta_r)_s / \lambda_S} \end{aligned} \right\} (3)$$

$$\left. \begin{aligned} (\delta_\theta)_w &= (\delta_\theta)_e = \Delta \theta \\ (\delta_r)_n &= (\delta_r)_s = \Delta r \end{aligned} \right\} a_P = a_W + a_E + a_N + a_S \quad (4)$$

By forwarding the index from i to $i + 1$, Eq. (2) is rewritten as

$$T(i+1, j) = \frac{a_P T(i, j) - [a_W T(i, j-1) + a_E T(i, j+1) + a_N T(i-1, j)] - b(i, j)}{a_S} \quad (5)$$

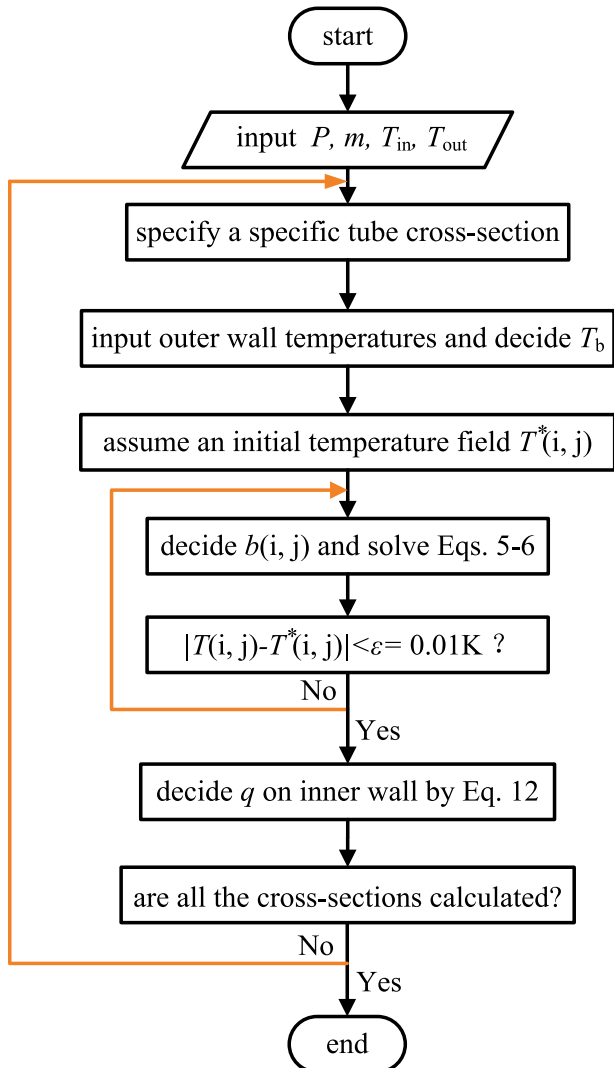


Fig. 5. The calculation procedure of the temperature field in silver domain and tube wall domain and the heat flux distribution on inner wall surface.

Eq. (5) is valid for $i = 2$ to $M_t - 1$, where M_t is on the inner wall surface. By applying the radial index forward method to the energy balance equation in the control volume $i = 1$ yields

$$T(2, j) = \frac{a_P T(1, j) - a_W T(1, j-1) - a_E T(1, j+1) - b(1, j)}{a_S} \quad (6)$$

where $a_W = \frac{\Delta r}{2r_0 \Delta \theta / \lambda_W}$, $a_E = \frac{\Delta r}{2r_0 \Delta \theta / \lambda_E}$, $a_S = \frac{r_s \Delta \theta}{\Delta r / \lambda_S}$, $a_P = a_W + a_E + a_S$ and $r_s = r_0 - 0.5 \Delta r$, noting that $T(1, j)$ is known which is measured by thermocouples.

Now, $b(i, j)$ in the silver layer domain and tube wall domain is determined:

$$R(i, j) = \frac{\rho_e(i, j)}{\Delta S(i, j)}, \quad b(i, j) = \frac{V_z^2}{R(i, j)} \quad (7)$$

where $R(i, j)$ is the electric resistance in control volume (i, j) , $\rho_e(i, j)$ is the specific resistance, which is determined by $T(i, j)$, $\Delta S(i, j)$ is the cross-section area of the grid, V_z is the voltage per unit length. The total resistance per unit length is R_t for silver layer and tube wall.

$$R_t = \left(\sum_{i=1}^{M_t} \sum_{j=1}^5 \frac{1}{R(i, j)} \right)^{-1} \quad (8)$$

Thus, the total heat generation per unit length is

$$Q_z = \frac{V_z^2}{R_t} \quad (9)$$

On the other hand, Q_z can also be determined based on the heat absorption in the scCO_2 side.

$$Q_z = \frac{m(i_{T_{\text{out}}} - i_{T_{\text{in}}})}{L} \quad (10)$$

where m is the mass flow rate of scCO_2 , i is the CO_2 enthalpy, T_{in} and T_{out} are the CO_2 temperatures entering and leaving the tube, respectively, L is the effective heating length. The numerator of Eq. (10) is the total heat absorption across the whole heating length. Combining Eqs. (7)–(10) yields

$$b(i, j) = \frac{R_t}{R(i, j)} \cdot \frac{m(i_{T_{\text{out}}} - i_{T_{\text{in}}})}{L} \quad (11)$$

Eqs. (5) and (6) subjected to Eq. (11) are solved by the TDMA method [38]. After the convergent temperatures are obtained, the inner wall heat flux is deduced as

$$q_w(M_t, j) = \frac{a_N T(M_t - 1, j) + a_W T(M_t, j + 1) + a_E T(M_t, j - 1) - a_P T(M_t, j) + b(M_t, j)}{r_i \Delta \theta} \quad (12)$$

where $a_W = \frac{\Delta r}{2r_i \Delta \theta / \lambda_W}$, $a_E = \frac{\Delta r}{2r_i \Delta \theta / \lambda_E}$, $a_N = \frac{r_n \Delta \theta}{\Delta r / \lambda_N}$, $a_P = a_W + a_E + a_N$. Eq. (12) reflects the energy conservation in the grey grid close to the inner wall surface (see Fig. 4d). The inner heat transfer coefficient is

$$h = \frac{q_w}{T_{w,i} - T_b} \quad (13)$$

where T_b is bulk fluid temperature, which is dependent on the bulk

Table 2
Parameter measurements and uncertainties.

Parameters	Range	Uncertainty
Pressure P	7.51–21.1 MPa	0.1%
P/P_{cr}	1.018–2.856	0.1%
Differential pressure ΔP	5.7–48.5 kPa	0.1%
T_{in}/T_{cr}	0.964–1.0358	0.5 °C
T_{out}/T_{cr}	0.9832–1.5551	0.5 °C
Mass flux G	488–1500 kg/m ² s	2.05%
Heating power Q	1.67–25.9 kW	3.25%
Heat flux q_w	43.7–488 kW/m ²	5.05%

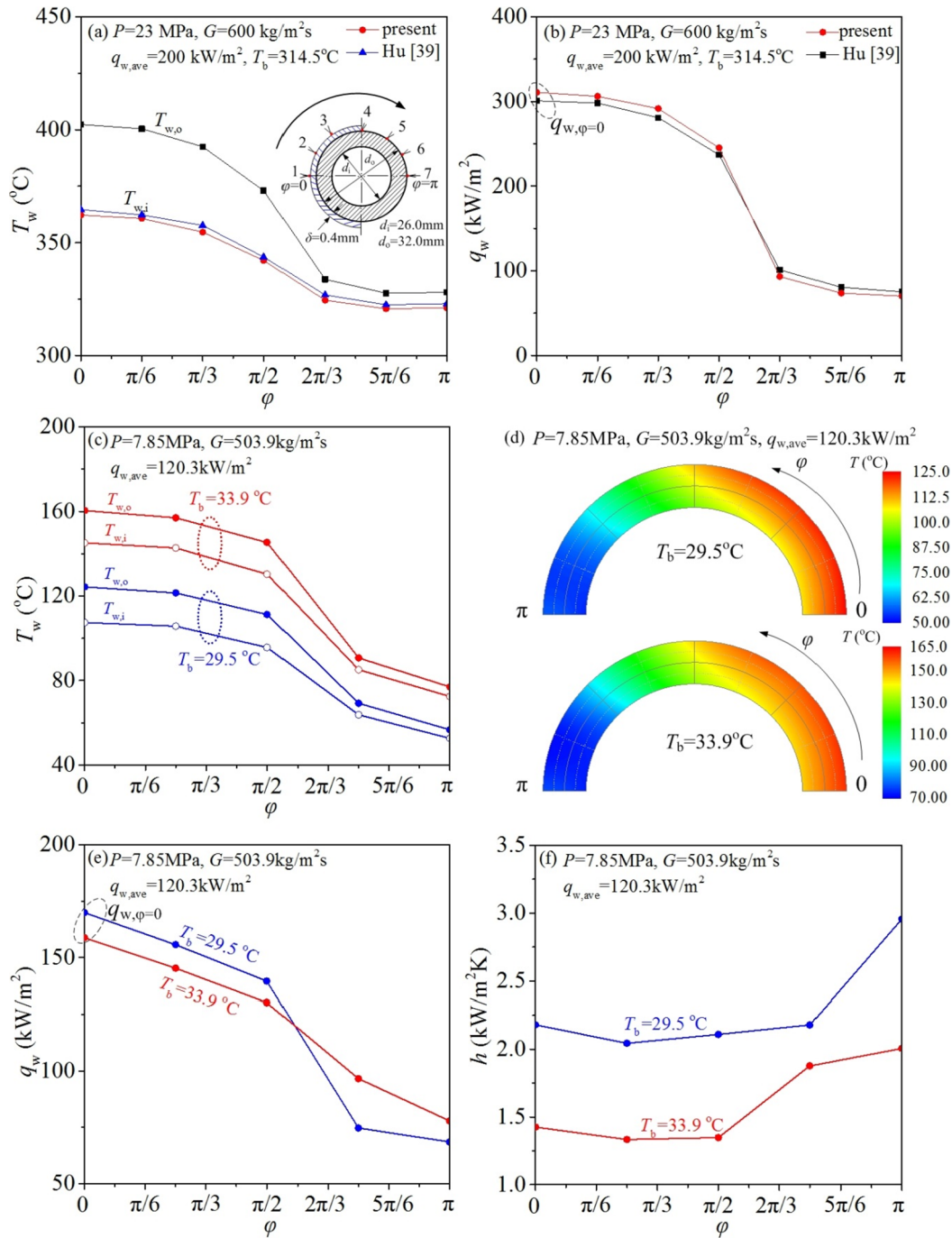


Fig. 6. Outcomes of inner wall heat fluxes and temperatures along circumference direction (a and b: comparison with other computations; c-f: calculations for our own scCO₂ data).

fluid enthalpy $i_b(z)$ along flow direction:

$$i_b(z) = i_{T_{in}} + \frac{(i_{T_{out}} - i_{T_{in}})z}{L} \quad (14)$$

where $i_{b,in}$ is inlet fluid enthalpy, z is the axial flow length starting from the first electrode.

The calculation procedure includes two levels of iteration: the first level for a specific axial location z , and the second level to scan different z , each corresponding to a specific tube cross-section (see Fig. 5). At a specific cross-section, T_b is determined according to Eq. (14). An initial temperature field is assumed. The internal heat source in each grid $b(i,$

$j)$ is determined by Eq. (11). Solving Eqs. (5) and (6) updates the temperature field. Such process continues until the convergent criterion is satisfied. Then, the inner wall heat flux is obtained by Eq. (12). The current iteration level stops, and a new level of iterations begins for another tube cross-section. In such a way, the temperature field and inner wall heat fluxes are determined along the whole tube length and circular angles.

The uniform heating case is treated in a similar way to the non-uniform heating case. The only difference is that for uniform heating, the heat generation is only contributed by the resistance heating of tube wall. We note that the material of 1Cr18Ni9Ti stainless steel has

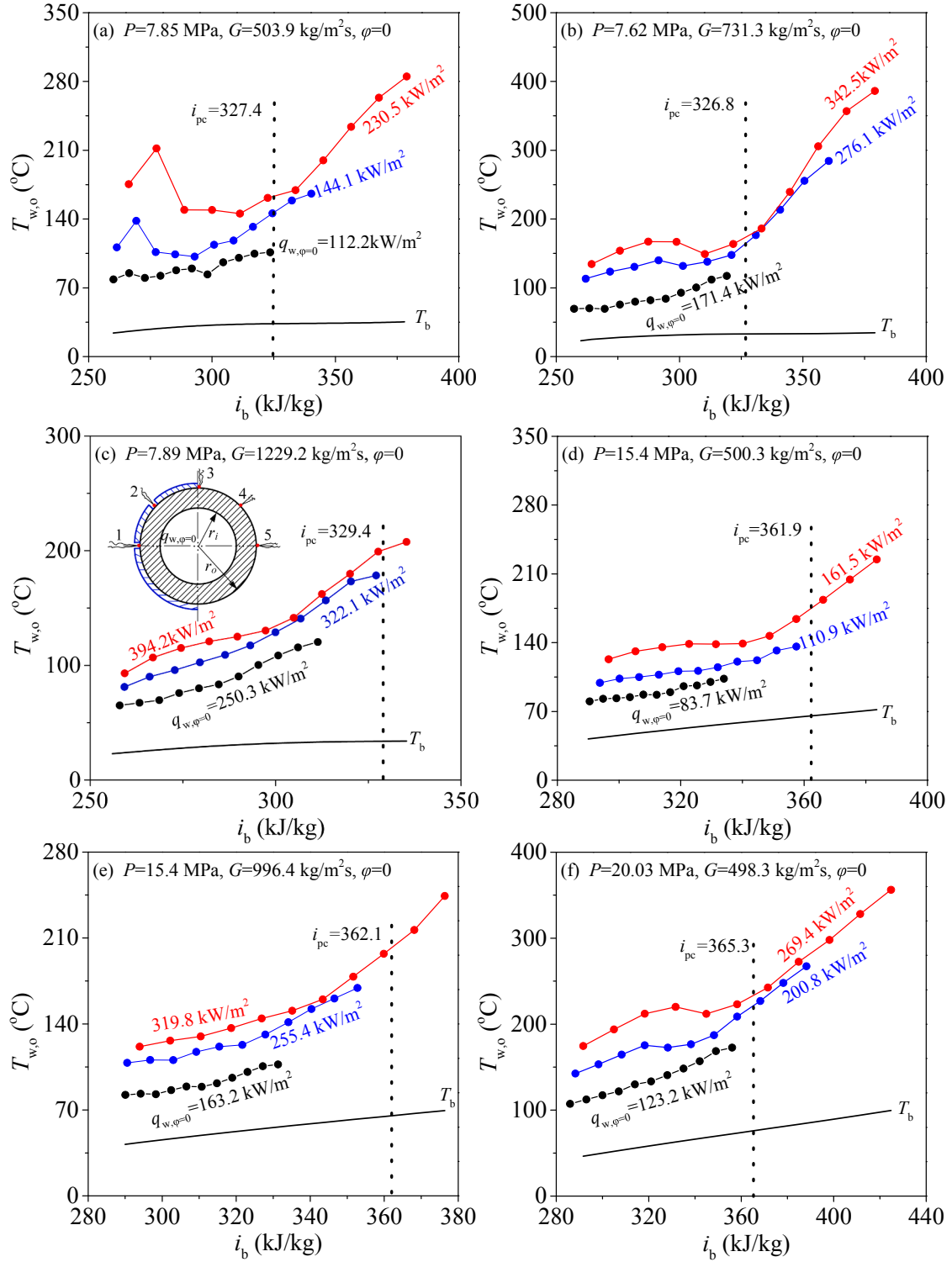


Fig. 7. Effect of heat fluxes on scCO₂ heat transfer.

temperature dependent physical properties. Thermal conductivity λ and specific resistance ρ_e are [39]:

$$\lambda = 14.3 + 0.0134T \quad (15)$$

$$\rho_e = 7.74 \times 10^{-7}(1.0 + 7.75 \times 10^{-4}T) \quad (16)$$

Our calculation shows that for uniform heating, the constant heat flux boundary condition is still valid due to the weak temperature

dependent specific resistance. For example, $T_{in} = 41.7 \text{ }^\circ\text{C}$, $T_{out} = 80.8 \text{ }^\circ\text{C}$, $G = 512.9 \text{ kg/m}^2\text{s}$ and $P = 15.632 \text{ MPa}$ give an average heat flux on inner wall of $q_{w,ave} = 77.24 \text{ kW/m}^2$. The calculation procedure based on Fig. 5 gives the heat fluxes of $q_{w,c} = 78.55 \text{ kW/m}^2$ at the entrance colder region and $q_{w,h} = 76.751 \text{ kW/m}^2$ at the ending hotter region, indicating that the relative difference among $q_{w,ave}$, $q_{w,c}$ and $q_{w,h}$ is smaller than 1.7%.

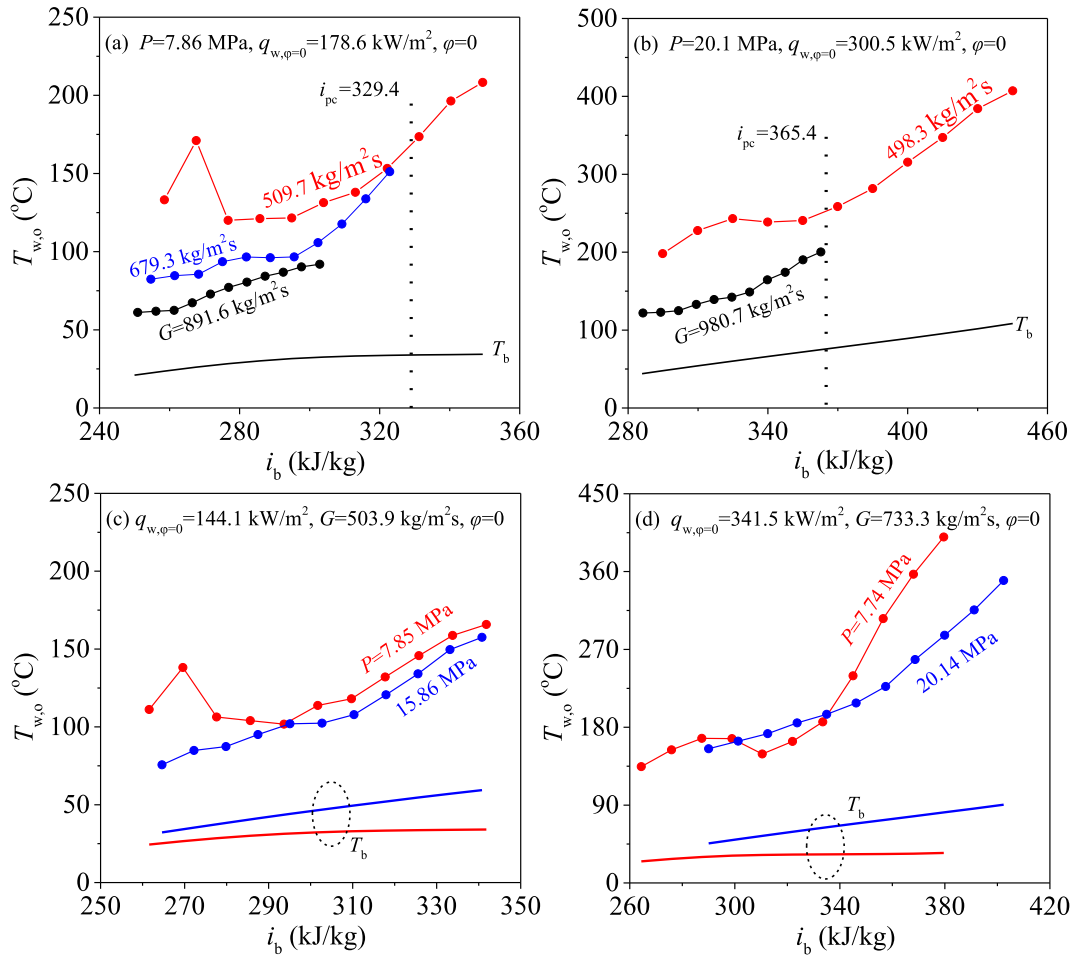


Fig. 8. Effects of mass fluxes and pressures on scCO₂ heat transfer.

2.4. Measurements and uncertainties

The mass flow rate is measured by one of the two Coriolis mass flow meters, DMF-1-3-B with a mass flow rate range of 0–1000 kg/h and DMF-1-2-A with a mass flow rate range of 0–200 kg/h, both having uncertainties of 0.2%. During operation, one of the two mass flow meters is selected by switching on one of the two valves. The fluid temperatures are measured by K-type jacket thermocouples with diameter of 1.0 mm. The wall temperatures are measured by thermocouple wires with diameter of 0.25 mm. After calibration, these thermocouples have maximum uncertainty of 0.5 °C. The Rosemount 3051 pressure transducer measures fluid pressures with an uncertainty of 0.2%. The Rosemount 1151 differential pressure transducer measures pressure drops with an uncertainty of 0.1%. To determine the heating power applied to the test tube, the DC (direct-current) voltage and current come from the readings of a voltage converter (0–5 V range) and a current converter (0–75 mA), respectively. The real voltage and current are linearly related to the two readings of the converters with two specific coefficients. All the signals are collected by a data acquisition system (ADAM-4118/4117) with an uncertainty of 0.2%. The uncertainties of heating power, heat flux and heat transfer coefficient are obtained using the error transmission principle. The above process gives the uncertainties of 3.25% for Q and 5.05% for q_w (see Table 2).

3. Results and discussion

3.1. Calibration of the data reduction process

Fig. 6a–b compares our calculated wall temperatures $T_{w,i}$ based on measured wall temperatures $T_{w,o}$, for supercritical water flowing in a vertical tube with $P = 23$ MPa, $G = 600$ kg/m²s, $q_{w,ave} = 200$ kW/m² and $T_b = 314.5$ °C. Our calculated $T_{w,i}$ and inner wall heat fluxes q_w match the computation results by Hu [39]. To further verify the correctness of our calculations of solid wall temperatures, we consider the solution of Eq. (1) for steady-state one-dimensional heat conduction problem with a uniform internal heat source. When adiabatic thermal boundary condition is applied on the outer wall, Eq. (1) has the theoretical solution of

$$T_{w,i} = T_{w,o} + \frac{S(d_o^2 - d_i^2)}{16\lambda} + \frac{Sd_o^2}{8\lambda} \ln \frac{d_i}{d_o} \quad (17)$$

For an example case of $S = 100 \times 10^6$ W/m³, $d_i = 10.0$ mm, $d_o = 14.0$ mm, $T_{w,o} = 200$ °C, $\lambda = 17.625$ W/m·K, Eq. (17) achieves $T_{w,i} = 189.35$ °C, which is exactly identical to the calculated $T_{w,i} = 189.35$ °C based on numerical simulation described in Section 2.3.

For non-uniform heating, the angle dependent parameters are shown in Fig. 6c–f at $P = 7.85$ MPa, $G = 503.9$ kg/m²s and $q_{w,ave} = 120.3$ kW/m². The outer tube wall is coated by silver layer with $\varphi = \left(-\frac{\pi}{2}, \frac{\pi}{2}\right)$, which is called hot-side-region (HSR). Due to the

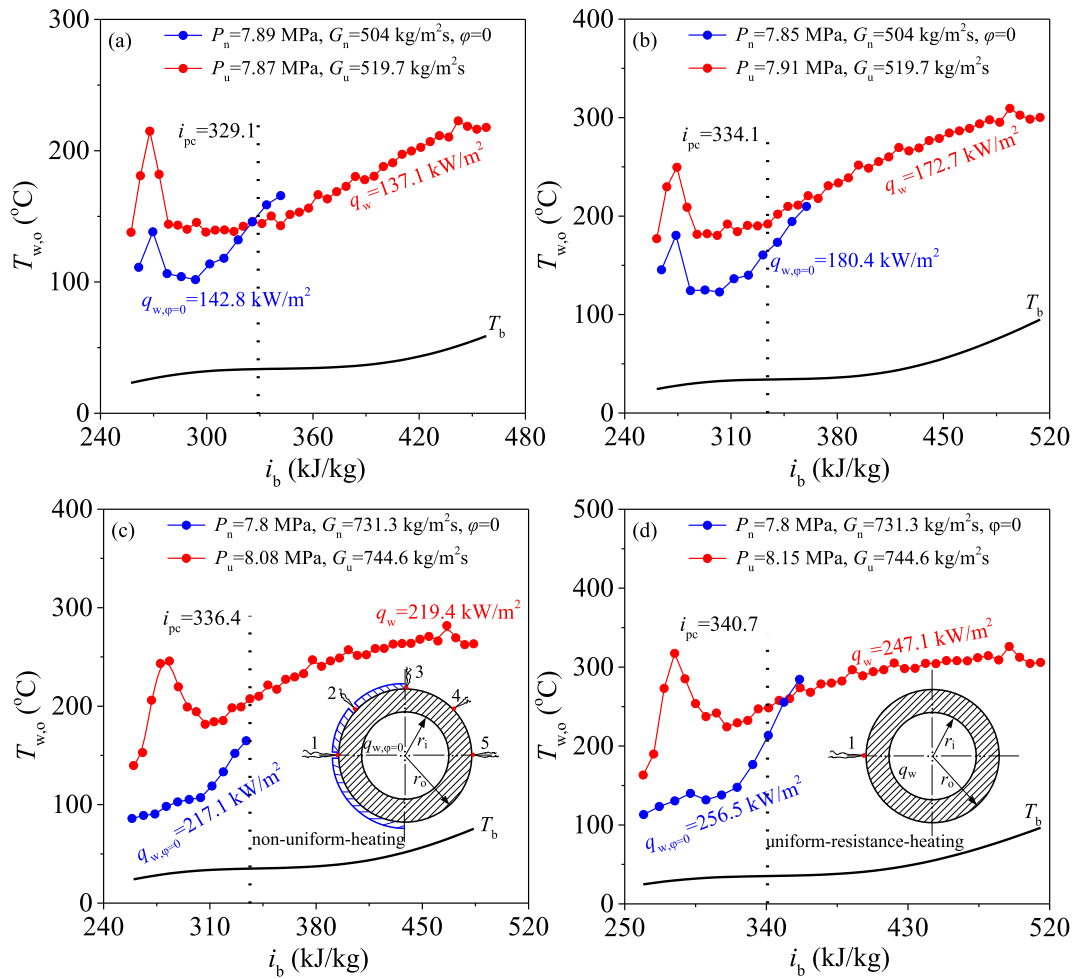


Fig. 9. Heat transfer performance between uniform heating (red curves) and non-uniform heating (blue curves) at near-critical pressure. (For interpretation of the references to colour in this figure legend, the reader is referred to the web version of this article.)

resistance heating and thermal conduction of tube, the inner wall in the range of $\varphi = \left(\frac{\pi}{2}, \frac{3\pi}{2}\right)$ also has heat fluxes, which is called cold-side-region (CSR). The tube temperatures and inner wall heat fluxes are higher in HSR, but sharply reduce in CSR (see Fig. 6c–e), in which Fig. 6d shows the tube wall temperature field in r - φ coordinates. One maybe interest in the distribution of heat transfer coefficients versus circumference angles (see Fig. 6f). HSR possesses lower heat transfer coefficients and the difference of h in this region is not large, but h sharply increases beyond $\varphi = \pi/2$ in CSR. The change trend of $h \sim \varphi$ is same for different bulk fluid temperatures T_b .

3.2. Effect of various parameters on $scCO_2$ heat transfer for non-uniform heating

Totally, 82 runs of $scCO_2$ heat transfer experiment are performed for non-uniform heating. Heat transfer performance is presented with $T_{w,o}$ at $\varphi = 0$ as the vertical coordinate and i_b as the horizontal coordinate. Fig. 7 deals with the effect of heat fluxes but Fig. 8 deals with the effects of mass fluxes and pressures. Near the critical pressure ~ 8 MPa, the lower heat fluxes such as $q_{w,\varphi=0} = 112.2 \text{ kW/m}^2$ in Fig. 7a, 171.4 kW/m^2 in Fig. 7b and 250.3 kW/m^2 in Fig. 7c keep gentle slope of $T_{w,o}$ versus i_b . The increase of heat fluxes may yield the occurrence of peak wall temperatures ahead of pseudo-critical point (see Fig. 7a at 230.5 kW/m^2). The gentle variation of $T_{w,o}$ versus i_b is called normal heat transfer NHT, and the peak wall temperature before pseudo-

critical point is called heat transfer deterioration HTD. By examining wall temperature curves at ~ 8 MPa in Fig. 7a–c, 15.4 MPa in Fig. 7d–e, and 20.03 MPa in Fig. 7f, the heat transfer is improved by increasing pressures.

Fig. 8a and b shows the effect of G on $scCO_2$ heat transfer. Smaller G such as $G = 509.7 \text{ kg/m}^2\text{s}$ demonstrates HTD, but higher G of $679.3 \text{ kg/m}^2\text{s}$ and $891.6 \text{ kg/m}^2\text{s}$ switch HTD to NHT (see Fig. 8a). Fig. 8c and d further illustrates the effect of pressures. Fig. 8c shows that higher pressure of 15.86 MPa eliminates the wall temperature peak compared to 7.85 MPa. Fig. 8d demonstrates that higher pressure of 20.14 MPa decreases the slope of wall temperatures compared to 7.74 MPa.

3.3. Effect of non-uniform heating on $scCO_2$ heat transfer

Figs. 9 and 10 illustrate the effect of non-uniform heating on $scCO_2$ heat transfer, dealing with both near critical pressure case and higher pressure case. The subscript u means uniform heating and n means non-uniform heating. Because it is difficult to keep exactly the same parameters, the differences of P , G and q_w (or $q_{w,\varphi=0}$) between the two heating modes are controlled to be within 5%. At same i_b , the small difference of pressures yields neglectable difference of bulk fluid temperatures T_b . Hence, only one $T_b \sim i_b$ curve is shown in Figs. 9 and 10.

The non-uniform heating delays or eliminates HTD. For example, the uniform heating with $q_w = 219.4 \text{ kW/m}^2$ displays strong wall

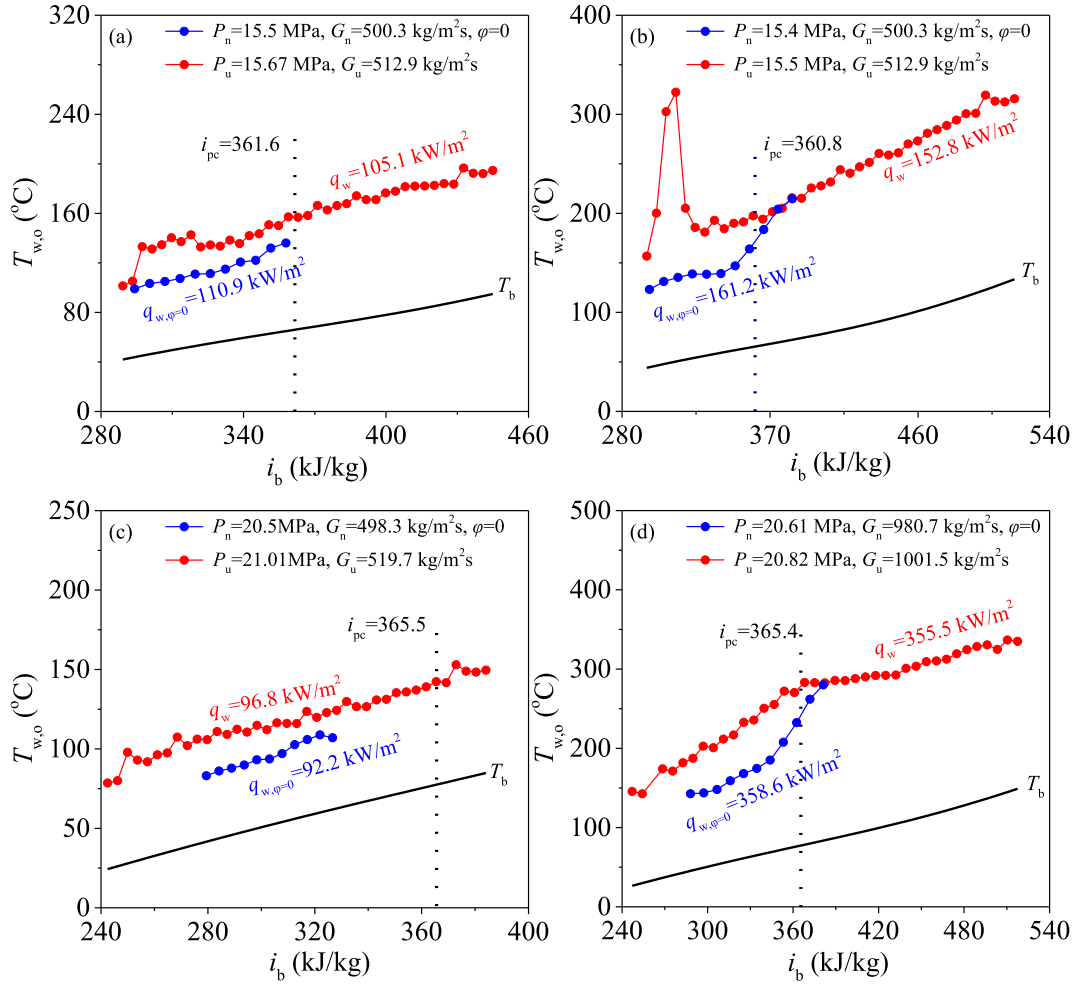


Fig. 10. Heat transfer performance between uniform heating (red curves) and non-uniform heating (blue curves) at pressures larger than critical pressure. (For interpretation of the references to colour in this figure legend, the reader is referred to the web version of this article.)

temperature peak, but the non-uniform heating with $q_{w, \phi=0} = 217.1 \text{ kW/m}^2$ does not have wall temperature peak (see Fig. 9c). Similar phenomenon is also observed at pressure $\sim 15 \text{ MPa}$ (see Fig. 10b). However, beyond pseudo-critical point, wall temperature curves can be crossing between the two heating modes for some cases (see Figs. 9a, b, d and 10b, d). The non-uniform heating has opposite effects on heat transfer in lower and higher enthalpies region. Because HTD always takes place before pseudo-critical point, the non-uniform heating improves the boiling-like heat transfer. However, after scCO_2 is heated to pure gas state, the non-uniform heating deteriorates heat transfer in higher enthalpy region. In other words, regarding the non-uniform heating effect, the heat transfer performance before and after pseudo-critical point belongs to different mechanisms. The former is related to the boiling-like mechanism, but the latter is dominated by the convective heat transfer with single-phase fluid only. The present paper focuses on the boiling-like heat transfer and HTD. The heat transfer characteristic beyond pseudo-critical point needs further investigation.

3.4. Pseudo-boiling theory and new non-dimensional parameter

As defined in textbooks, it is impossible to identify liquid from gas beyond critical point, thus only a single phase is defined [32]. The phase diagram includes a subcritical region with two-phases of liquid and gas, and a supercritical region containing single-phase (see Fig. 11a). At subcritical pressure, the latent heat of evaporation (i_{ig})

determines the heat to convert liquid to vapor at a saturation temperature. At supercritical pressure, the pseudo-critical point pc is defined at maximum specific heat, whose location shifts to higher temperature when increasing pressure. Heat transfer to supercritical fluid cannot take place at a constant temperature, but causes a temperature rise. The single-phase concept and the buoyancy/acceleration effect has been used to explain and correlate the supercritical heat transfer (SHT) for a long time.

The single-phase concept is questioned by physicists in recent years. The two regimes of liquid-like fluid and gas-like fluid are shown in Fig. 11b for scCO_2 . The Widom line beyond critical point is determined using the maximum specific heat, matching the prediction of $P/P_{cr} = \exp[5.55(T/T_{cr} - 1)]$ suggested by Banuti [40]. Even though the pseudo-boiling concept was mentioned by earlier investigators in their experiments [41], the theory has not been incorporated into the theoretical analysis of SHT.

Here, the pseudo-boiling concept is introduced to deal with SHT, which is explained using the c_p curve near pseudo-critical point (see Fig. 11c). The transition from liquid-like fluid to vapor-like fluid occurs at the Widom line, matching the pseudo-critical temperature T_{pc} [40]. “Boiling” occurs in a temperature range from $T^- < T_{pc}$ to $T^+ > T_{pc}$. The energy for “boiling” from liquid-like fluid to vapor-like fluid is

$$\Delta i = \int_{T^-}^{T^+} c_p(T) dT = i(T^+) - i(T^-) = \Delta i_{sen} + \Delta i_{pt} \quad (18)$$

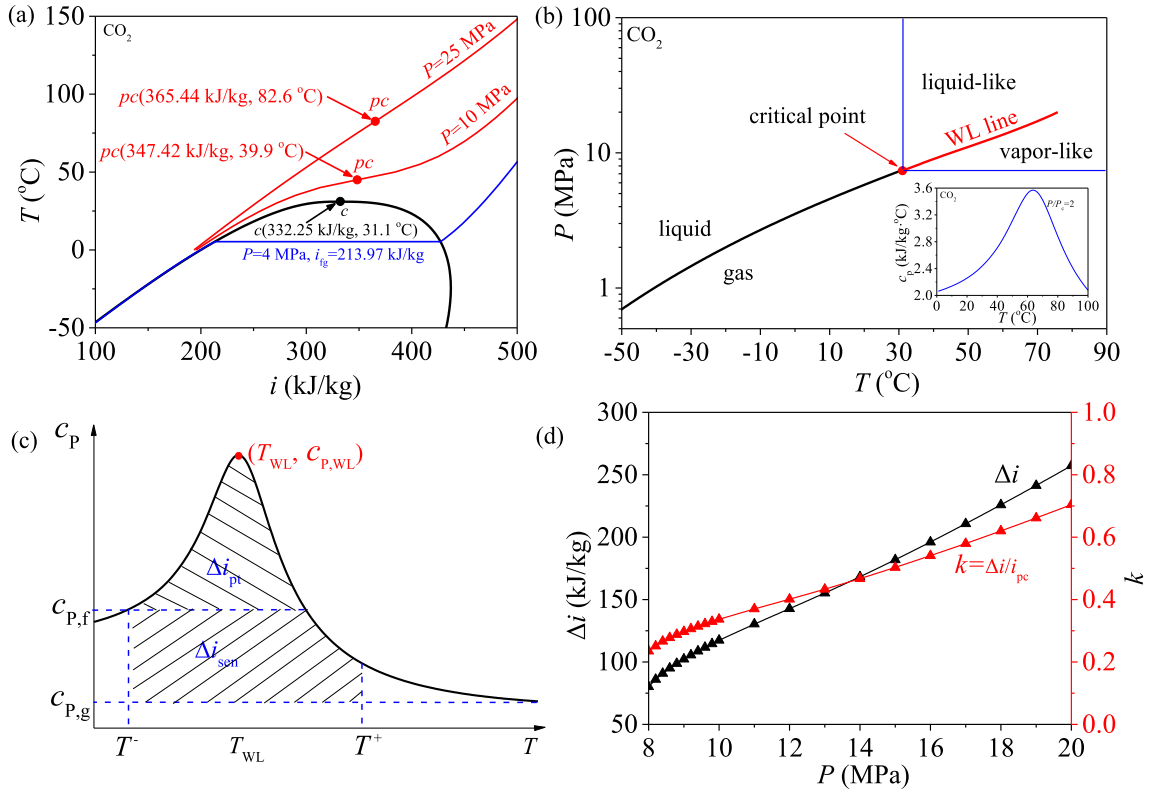


Fig. 11. Thermodynamics and heat transfer behavior at subcritical and supercritical pressures: (a) T - i curves at different pressure levels to show isothermal two-phase regime at subcritical pressure and temperature rise at supercritical pressure; (b) P - T curves characterize the transition from liquid to vapor at subcritical pressures and from liquid-like fluid to gas-like fluid at supercritical pressures; (c) c_p curve near the Widom line coincided with the pseudo-critical point pc [40]; (d) pseudo-boiling enthalpy Δi and k .

The energy can be divided into two parts [40]. The first part Δi_{sen} contributes a temperature rise from T^- to T^+ , and the second part Δi_{pt} overcomes the molecular attraction to achieve the vapor-like fluid. This differs from the subcritical boiling, under which a constant temperature is kept and all the energy is used for phase change. The determination of T^- and T^+ can be found in Refs. [40,42]. Both Δi and $k = \Delta i/i_{pc}$ increases with increase of pressures, where i_{pc} is the enthalpy at pseudo-critical point. Corresponding to $P = 8$ – 20 MPa, the range of 0.235 – 0.704 for k indicates that Δi and i_{pc} are in the same magnitude (see Fig. 11d).

SHT is analogized to subcritical boiling. Bubbles nucleate and grow on the wall, detaching the wall to merge. Then, they are condensed by the sub-cooled liquid of tube core, yielding no net vapor generation there. If the bubbles do not detach the wall, they merge to form a vapor blanket. From t to $t + \Delta t$, the evaporation at a bubble interface induces a mass transfer from liquid to vapor, resulting in an increase of bubble volume ΔV . Due to bubble expansion, a force F_{Ml} is exerted on the surrounding liquid of bubble. An anti-force F_{Mv} is applied on the bubble, which is called the evaporation momentum force [43] (see Fig. 12a and b).

$$F_{Ml} = \left(\frac{q_w}{i_{fg}} \right)^2 \frac{D}{\rho_g} \quad (19)$$

where D is the bubble diameter and ρ_g is the vapor density. The inertia force applied on the bubble interface is

$$F_{\Gamma} = \frac{G^2 D}{\rho_l} \quad (20)$$

where ρ_l is the liquid density. The K number reflects the evaporation

momentum force competed with the inertia force, dominating if bubbles can detach the wall:

$$K = \frac{F_{Ml}}{F_{\Gamma}} = \left(\frac{q_w}{Gi_{fg}} \right)^2 \frac{\rho_l}{\rho_g} = \frac{\rho_l}{\rho_g} Bo^2 \quad (21)$$

where Bo is the boiling number: $Bo = q_w/(Gi_{fg})$.

Now, we deal with supercritical heat transfer (see Fig. 12c and d). A thin vapor layer behaves $T_{w,i} > T_{pc} > T_b$, where $T_{w,i}$ is the inner wall temperature. Beyond the Widom line is the core flow with higher fluid density, which is treated as “subcooled” liquid due to $T_b < T_{pc}$. The Widom line is considered as “saturation temperature”. Evaporation on the Widom line generates a vapor mass increment to expand the vapor layer thickness. The evaporation is caused by heating from superheated vapor to saturation liquid across the Widom line. The vapor expansion causes a momentum force on the Widom line. If the inertia force is sufficiently large to suppress the evaporation momentum force, the vapor layer becomes thinner to keep normal heat transfer (NHT). If the inertia force is smaller compared to the evaporation momentum force, the vapor layer grows significantly to cause heat transfer deterioration (HTD).

The enthalpy Δi should be defined for “boiling” from liquid-like fluid to vapor-like fluid. Eq. (18) indicates Δi dependent on T^- and T^+ . To avoid the determination of T^- and T^+ , Δi can be decided by introducing k (see Fig. 11d):

$$\Delta i = i(T^+) - i(T^-) = k \cdot i_{pc} \quad (22)$$

Hence, the evaporation mass flux on the Widom line is scaled as $q_w/\Delta i$ and q_w/i_{pc} . The analogy between subcritical boiling and SHT creates supercritical-boiling-number as

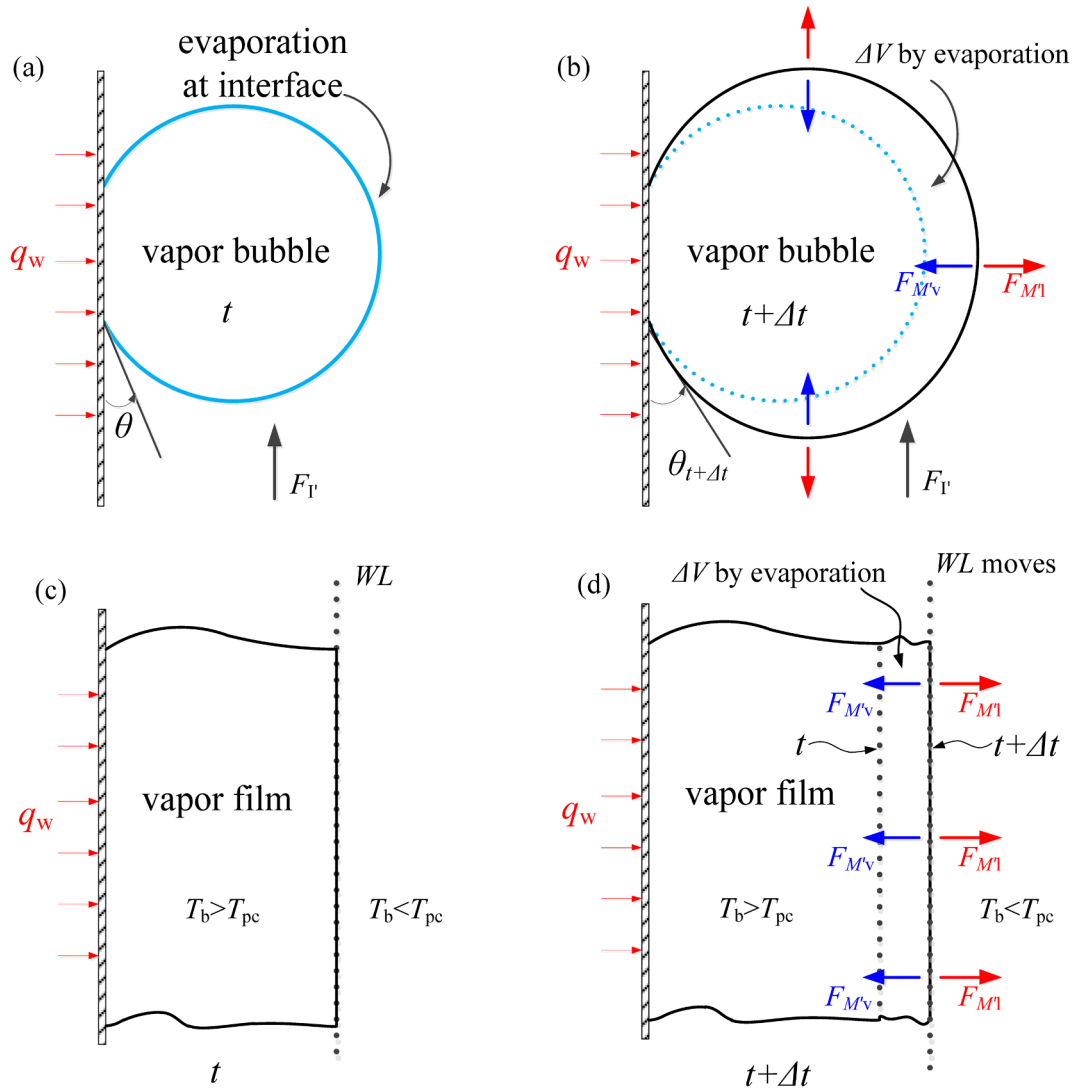


Fig. 12. Similarities of boiling at subcritical pressure and supercritical heat transfer (a and b: subcritical pressure case; c and d: supercritical pressure case).

$$SBO = \frac{q_w}{G_{i_{pc}}} \quad (23)$$

3.5. The experiment determined criterion for onset of HTD

Some authors confirmed the occurrence of HTD if the following criterion is satisfied [4,11,15]

$$h/h_{D-B} < 0.3 \text{ or } 0.5 \quad (24)$$

where h is the practical heat transfer coefficient, h_{D-B} is the Dittus-Boelter heat transfer coefficient:

$$h_{D-B} = \frac{\lambda_b}{d_i} \cdot 0.023 Re_b^{0.8} Pr_b^{0.4} \quad (25)$$

where λ_b is the thermal conductivity of working fluid, Re_b and Pr_b are the Reynolds number and Prandtl number, respectively. Because it is possible for normal heat transfer to satisfy the criterion given by Eq. (24), other authors [5] queried the above criterion. Alternatively, HTD is identified by the wall temperature peak [5–7].

Fig. 13 shows the identification method (see Fig. 13a for NHT and Fig. 13b–d for HTD). The definition of HTD is paid attention. A temperature triangle apb exists, where p refers to the peak point. The lines

ap and pb represent the sharp rise route and the recovery route, respectively. The line ab is referenced as a normal heat transfer route. A temperature overshoot ΔT quantifies the deviation of the peak temperature from the normal heat transfer route. Usually, ΔT is very large when HTD occurs (see $\Delta T = 30.5, 76.5,$ and 147.6 °C in Fig. 13b–d). In this paper, $\Delta T > 8$ °C is the criterion to judge HTD. According to this criterion, among the 82 experimental runs for non-uniform heating, 53 runs are classified as NHT and the left 29 runs belong to HTD. We observe that few NHT runs also display weak peak but ΔT is only several degrees. The 8 °C limit, instead of zero, can avoid the wrong classification between NHT and HTD. The 8 °C limit is used for both non-uniform heating and uniform heating.

Fig. 14a–c presents $q_{w,q=0} \sim G$ curves at ~ 8 MPa, ~ 15 MPa and ~ 20 MPa, respectively. At similar pressures, the transition from NHT to HTD obeys the linear law. The increase of pressures suppresses the slopes of $q_{w,q=0}$ with respect to G , indicating the improved heat transfer by increasing pressures. The regime map is replotted in Fig. 14d with $G_{i_{pc}}$ as the horizontal coordinate. Different pressures have different T_{pc} and i_{pc} . For example, the 10 MPa pressure has $T_{pc} = 39.9$ °C and $i_{pc} = 347.42$ kJ/kg, but $P = 25$ MPa has $T_{pc} = 82.6$ °C and $i_{pc} = 365.44$ kJ/kg. Surprisingly, the transition from NHT to HTD shrinks to a single line for different pressures. We note that

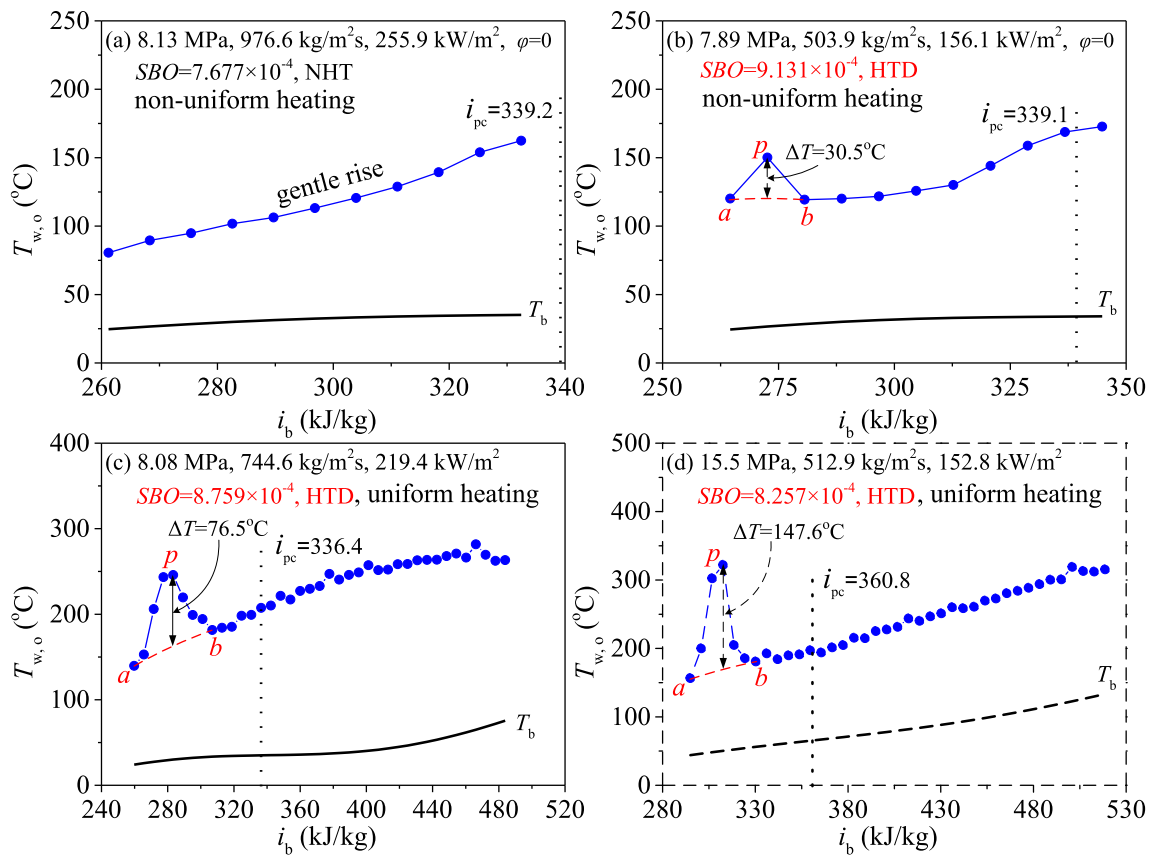


Fig. 13. Definition of heat transfer deterioration.

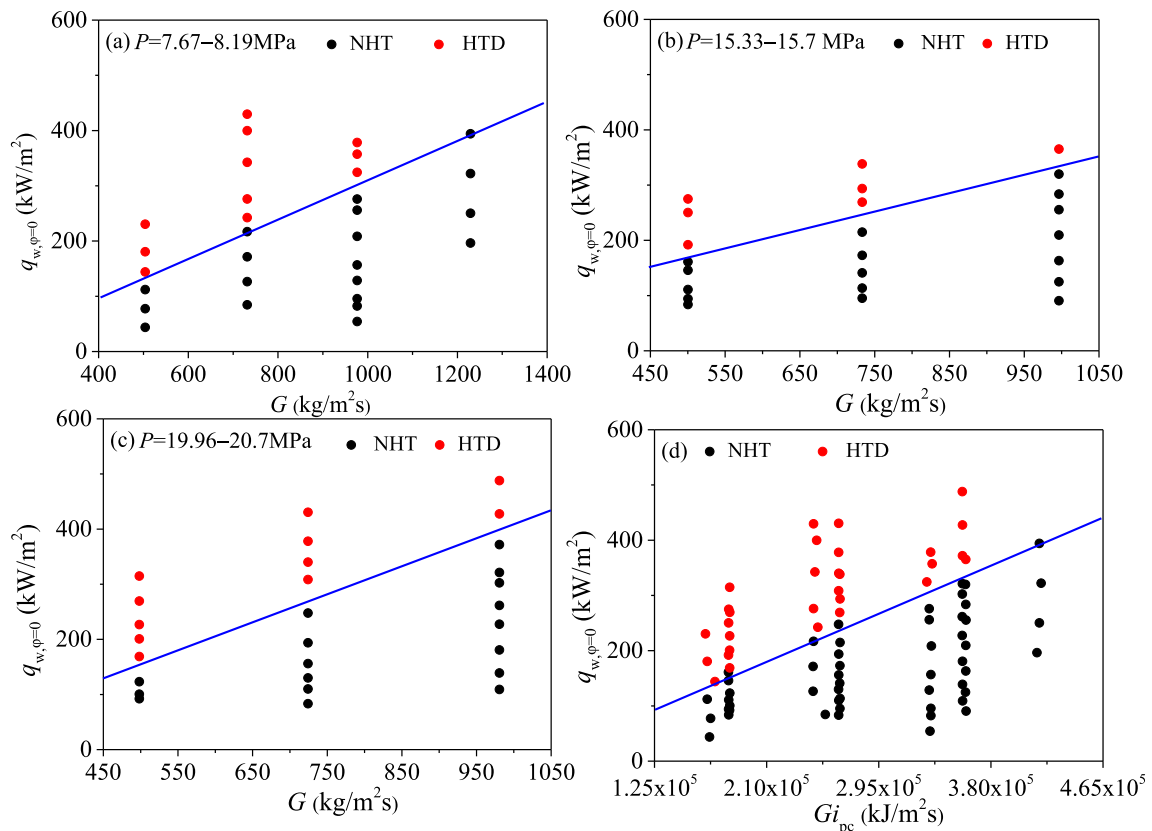


Fig. 14. Transition boundary between NHT and HTD (a: data at near critical pressure; b: data at $P = 15.33\text{--}15.7$ MPa; c: data at $P = 19.96\text{--}20.7$ MPa; d: transition boundary plotted with $q_{w,\phi=0}$ versus Gi_{pc}).

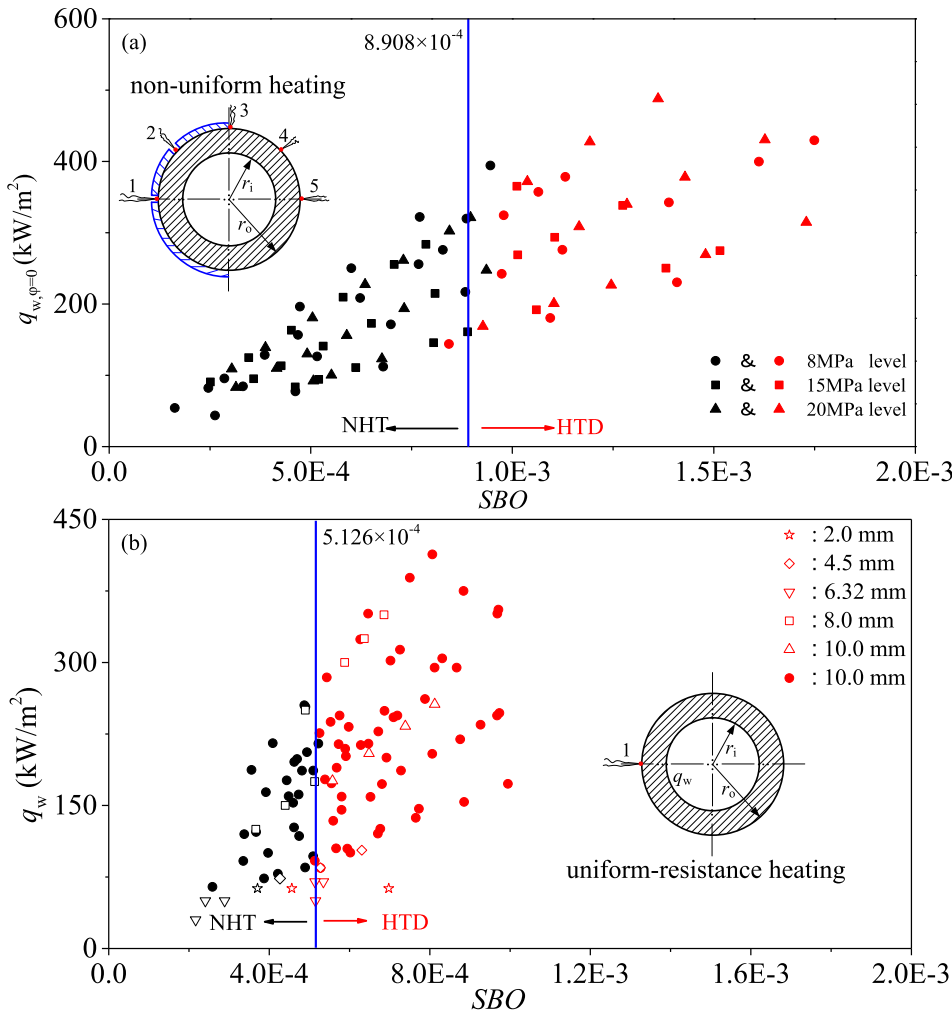


Fig. 15. The SBO number dominates the transition from NHT to HTD (a: non-uniform heating results; b: uniform heating results.) ● & ● our own data; ☆ & ☆ from Ref. [30] with 7.6 MPa/255–480 kg/m²s/63 kW/m²/2.0 mm; ◇ & ◇ from Ref. [45] with 7.532–8.194 MPa/488–492 kg/m²s/73.5–103.1 kW/m²/4.5 mm; ▽ & ▽ from Ref. [44] with 7.75–8.12 MPa/285–600 kg/m²s/30–70 kW/m²/6.32 mm; □ & □ from Ref. [46] with 8.35 MPa/1004–1502 kg/m²s/125–350 kW/m²/8.0 mm; △ & △ from Ref. [29] with 7.61 MPa/901.8 kg/m²s/175.9–256.2 kW/m²/10.0 mm).

the slope of the $q_{w,\varphi=0} \sim Gi_{pc}$ curve is the supercritical-boiling-number SBO defined in Eq. (23). This finding inspires us to replot Figs. 14d in 15a. Sudden change of heat transfer behaviors is found when crossing a critical $SBO_{cr} = 8.908 \times 10^{-4}$. Indeed, the transition from NHT to HTD is not controlled by heat flux alone, but dominated by SBO .

Fig. 15b presents the outcomes of uniform heating, including 79 data points from our experimental data ($d_i = 10$ mm), and 22 data points with other tube sizes [29,30,44–46]. The database covers wide range of pressures. The transition from NHT to HTD takes place at a critical $SBO_{cr} = 5.126 \times 10^{-4}$. It is seen that both uniform and non-uniform heating support the conclusion that HTD is dominated by SBO . Compared to uniform heating, non-uniform heating keeps larger SBO_{cr} . We recall that uniform heating creates symmetric-saddle-shape axial velocity profiles over tube cross-section [3,16]. However, non-uniform heating deforms the velocity profile to be asymmetric (see Fig. 16). Hence, the hotter side fluid has larger axial velocities than the colder side. The asymmetric velocity profile causes enhanced inertia effect to weaken the vapor layer thickness on the hotter side, explaining why the non-uniform heating delays the occurrence of HTD.

Based on Eq. (23), the critical heat flux (CHF) is defined for supercritical heat transfer deterioration:

$$q_{w,CHF} = SBO_{cr} \cdot G \cdot i_{pc} \quad (26)$$

where SBO_{cr} is 5.126×10^{-4} for uniform heating and 8.908×10^{-4} for non-uniform heating. CHF is linearly related to G and i_{pc} . In Eq. (26), G , i_{pc} and $q_{w,CHF}$ have the units of kg/m²s, kJ/kg and kW/m²,

respectively. Eq. (26) is called the linear law of supercritical heat transfer. The heater is safe if $q_w < q_{w,CHF}$. Otherwise, the heater is not safe.

3.6. Comparison with other studies and comments on SBO

Available works emphasize the importance of varied physical properties and buoyancy/acceleration effects on supercritical heat transfer. Huang and Li [23] emphasizes the inconsistencies of SHT, due to the not properly treated buoyancy effect. Hall and Jackson [47] proposed the Bu number to characterize the buoyancy effect:

$$Bu = \frac{Gr}{Re_b^{2.7}} \quad (27)$$

$$\left. \begin{aligned} Gr &= \frac{g \rho_b (\rho_b - \rho_{ave}) d_i^3}{\mu_b^2} \\ Re_b &= \frac{G d_i}{\mu_b} \\ \rho_{ave} &= \frac{\int_b^{T_w} \rho dT}{T_w - T_b} \end{aligned} \right\} \quad (28)$$

They state that the buoyancy effect is significant when $Bu > 10^{-5}$, but it can be neglected when $Bu < 10^{-5}$. Jackson [48] presented a modified Bu^* as

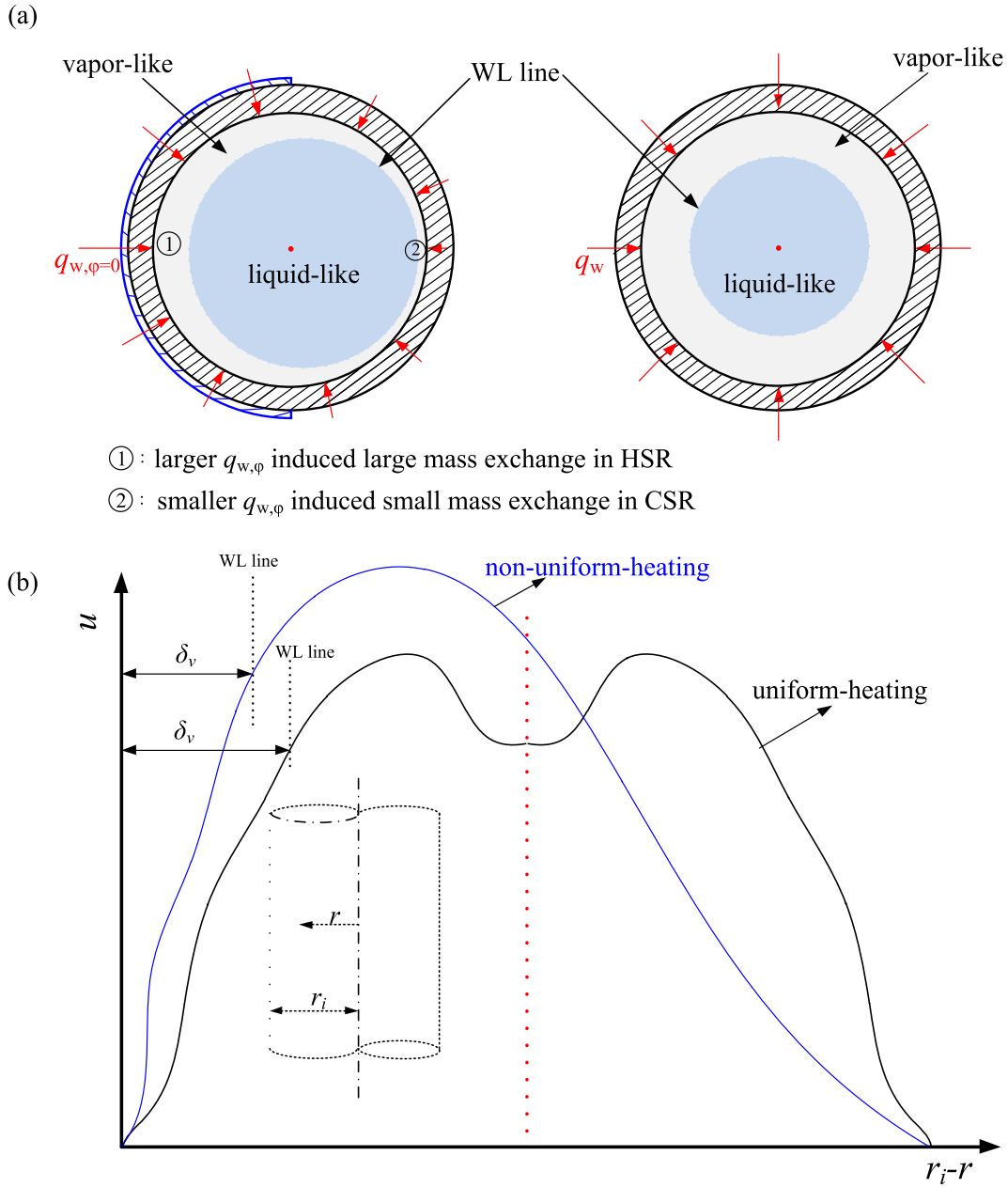


Fig. 16. The mechanism for heat transfer deterioration: a comparison between non-uniform heating and uniform heating.

$$Bu^* = \frac{Gr^*}{Re_b^{3.425} Pr_b^{0.8}} \quad (29)$$

$$Gr^* = \frac{g\beta_b d_i^4 q_w}{\nu_b^2 \lambda_b}, \quad Re_b = \frac{Gd_i}{\mu_b}, \quad Pr_b = \frac{\mu_b c_p}{\lambda_b} \quad (30)$$

He pointed out that the buoyancy effect is important when $Bu^* > 5.6 \times 10^{-7}$, but is weak when $Bu^* < 5.6 \times 10^{-7}$. We examine all the experimental data in Fig. 17a and b for uniform heating and Fig. 17c and d for non-uniform heating. The red color and black color represent HTD and NHT, respectively. It is seen that both criteria for buoyancy effect $Bu = 10^{-5}$ and $Bu^* = 5.6 \times 10^{-7}$ cannot judge the occurrence of HTD. HTD can take place for weak buoyancy effect, it can also take place for strong buoyancy effect. There is no direct connection between HTD and the buoyancy effect intensity. This is the reason why we abandon the buoyancy effect to deal with supercritical heat transfer.

Cheng et al. [15] proposed the following equation to predict the critical heat flux at supercritical pressures

$$\frac{q_{w,CHF}\beta_{pc}}{Gc_{p,pc}} = 1.354 \times 10^{-3} \quad (31)$$

where β_{pc} is the expansion coefficient, $c_{p,pc}$ is the specific heat at pseudo-critical point. For uniform heating, Fig. 18a plots the experimental data of our own and others in the literature, and the transition line predicted by Eq. (31). The experimental data classifying NHT and HTD roughly match the predictions by Eq. (31). However, eight data points belonging to HTD are predicted as NHT by Eq. (31). For non-uniform heating, the situation becomes more worse when comparing our experimental data with Eq. (31) (see Fig. 18b). In the right side of the transition line, sixteen experimental data points belonging to NHT are predicted as HTD by Eq. (31). Eq. (31) underpredicts $scCO_2$ heat

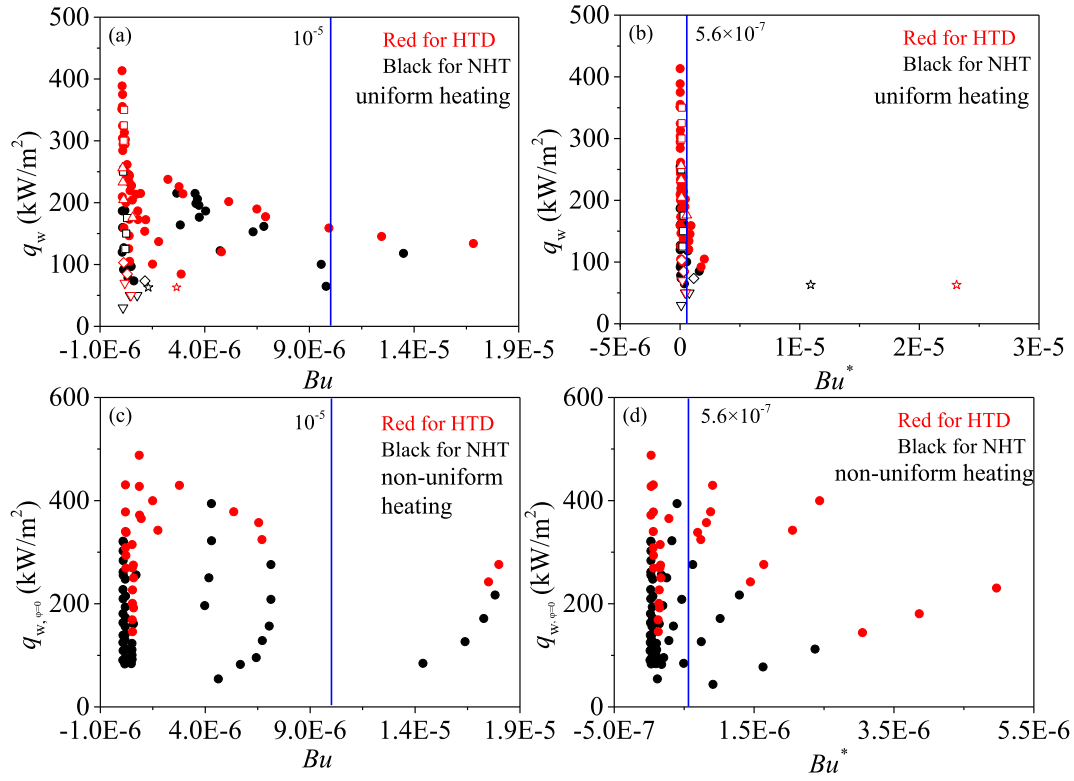


Fig. 17. Effect of buoyancy effect on heat transfer deterioration (a-b: uniform-heating results; c-d: non-uniform heating results.) ● & ● our own data; ☆ & ☆ from Ref. [30] with 7.6 MPa/255–480 kg/m²s/63 kW/m²/2.0 mm; ◇ & ◇ from Ref. [45] with 7.532–8.194 MPa/488–492 kg/m²s/73.5–103.1 kW/m²/4.5 mm; ▽ & ▽ from Ref. [44] with 7.75–8.12 MPa/285–600 kg/m²s/30–70 kW/m²/6.32 mm; □ & □ from Ref. [46] with 8.35 MPa/1004–1502 kg/m²s/125–350 kW/m²/8.0 mm; △ & △ from Ref. [29] with 7.61 MPa/901.8 kg/m²s/175.9–256.2 kW/m²/10.0 mm).

transfer for non-uniform heating.

ScCO₂ heat transfer is not dependent on a single parameter, but dependent on *SBO*, in which q_w/i_{pc} scales mass transfer from liquid-like fluid to vapor-like fluid, G quantifies the effect of inertia force. A smaller q_w/i_{pc} and/or larger G yield smaller *SBO* to keep NHT. The effect of pressures is implicitly reflected by i_{pc} . When pressure increases, the same energy decreases the mass transfer on the WL line to suppress the vapor layer growth. Hence, heat transfer is enhanced. The effect of d_i on heat transfer is complicated [49]. For uniform heating, the heat transfer regime map contains the data with $d_i = 2$ mm, 4.5 mm, 6.3 mm, 8 mm and 10 mm. The tube diameters do influence heat transfer coefficients, but do not influence the occurrence of HTD. The effect of d_i on scCO₂ heat transfer for non-uniform heating will be examined in the future. In summary, the current theory emphasizing the physical properties variation cannot predict scCO₂ heat transfer [23,24], but the problem can be treated by the pseudo-boiling theory and supercritical-boiling-number *SBO*.

When *SBO* exceeds a critical value, the vapor layer grows sharply to induce HTD. For non-uniform heating, the local *SBO* is

$$SBO_{\varphi} = \frac{q_{w,\varphi}}{Gi_{pc}} \quad (32)$$

Because the hot-side-region (HSR) receives heat from both the silver layer and tube material, but the cold-side-region (CSR) receives heat from the tube material only, HSR has larger $q_{w,\varphi}$ than CSR. We note that $q_{w,\varphi}/i_{pc}$ scales the mass transfer from liquid-like fluid to vapor-like fluid, HSR keeps larger mass transfer to thicken the vapor layer than CSR. Thus, HSR has lower heat transfer coefficients than CSR (see Fig. 6).

4. Conclusions

Following conclusions are drawn in this paper:

- ScCO₂ heat transfer experiments are performed for uniform heating and non-uniform heating. The maximum pressures are up to three times of the critical pressure. For non-uniform heating, the inner wall heat fluxes and heat transfer coefficients are strongly dependent on circumference angles. The hot-side-region has higher heat fluxes and lower heat transfer coefficients than the cold-side-region.
- Our experiments show that heat transfer is improved by increasing pressures. Compared to uniform heating, non-uniform heating has better performance ahead of pseudo-critical point and delays the occurrence of HTD, but worsens the heat transfer beyond pseudo-critical point.
- Supercritical heat transfer is dealt with by introducing pseudo-boiling. The added heat is decoupled into a temperature rise part and a phase change part. The flow consists of a vapor-like fluid near tube wall and a liquid-like fluid in tube core. The analogy between subcritical boiling and supercritical heat transfer results in a supercritical-boiling-number to govern the vapor layer growth.
- Two heat transfer regime maps are established. Sudden changes from normal heat transfer to heat transfer deterioration are found when crossing a critical *SBO*, which is 5.126×10^{-4} for uniform heating and 8.908×10^{-4} for non-uniform heating. The criterion number helps to avoid the heat transfer deterioration induced burn-out.
- The pseudo-boiling and supercritical-boiling-number explain the circumference angles dependent heat transfer behavior and the delayed HTD by non-uniform heating compared to uniform heating.

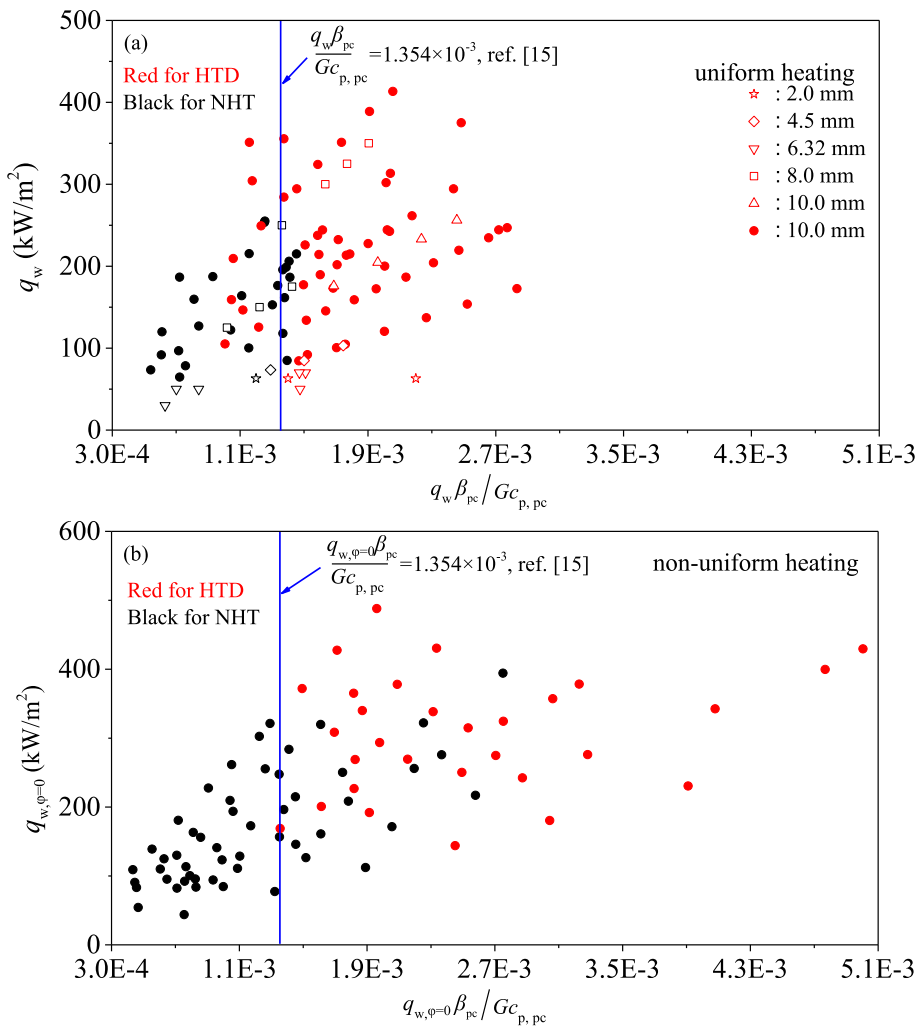


Fig. 18. Transition boundary from NHT to HTD predicted by the criterion in Ref. [15] (a: uniform-heating results; b: non-uniform heating results). ● & ● our own data; ☆ & ☆ from Ref. [30] with 7.6 MPa/255–480 kg/m²s/63 kW/m²/2.0 mm; ◇ & ◇ from Ref. [45] with 7.532–8.194 MPa/488–492 kg/m²s/73.5–103.1 kW/m²/4.5 mm; ▽ & ▽ from Ref. [44] with 7.75–8.12 MPa/285–600 kg/m²s/30–70 kW/m²/6.32 mm; □ & □ from Ref. [46] with 8.35 MPa/1004–1502 kg/m²s/125–350 kW/m²/8.0 mm; △ & △ from Ref. [29] with 7.61 MPa/901.8 kg/m²s/175.9–256.2 kW/m²/10.0 mm).

Declaration of Competing Interest

The authors declare that they have no known competing financial interests or personal relationships that could have appeared to influence the work reported in this paper.

Acknowledgements

The study was supported by the National Key R&D Program of China (2017YFB0601801), the National Natural Science Foundation of China (51821004).

References

- M. Pizzarelli, The status of the research on the heat transfer deterioration in supercritical fluids: A review, *Int. Commun. Heat. Mass.* 4 (2018) 132–138, <https://doi.org/10.1016/j.icheatmasstransfer.2018.04.006>.
- X.F. Kong, H.X. Li, Q. Zhang, K.K. Guo, Q. Luo, X.L. Lei, A new criterion for the onset of heat transfer deterioration to supercritical water in vertically-upward smooth tubes, *Appl. Therm. Eng.* 151 (2019) 66–76, <https://doi.org/10.1016/j.applthermaleng.2019.01.077>.
- J.M. Liu, Y.X. Jin, P.H. Zhao, Z.H. Ge, Y.J. Li, Y.X. Wan, Analysis of heat transfer of supercritical water by direct numerical simulation of heated upward pipe flows, *Int. J. Therm. Sci.* 138 (2019) 206–218, <https://doi.org/10.1016/j.ijthermalsci.2018.12.028>.
- D.L. Ma, T. Zhou, Bing, A.S. Li, Y.P. Huang Muhammad, An improved correlation on the onset of heat transfer deterioration in supercritical water, *Nucl. Eng. Des.* 326 (2018) 290–300, <https://doi.org/10.1016/j.nucengdes.2017.11.026>.
- Q. Zhang, H.X. Li, X.L. Lei, J. Zhang, X.F. Kong, Study on identification method of heat transfer deterioration of supercritical fluids in vertically heated tubes, *Int. J. Heat. Mass. Transf.* 127 (2018) 674–686, <https://doi.org/10.1016/j.ijheatmasstransfer.2018.07.058>.
- W.Q. Zhang, H.X. Li, Q. Zhang, X.L. Lei, Q. Zhang, Experimental investigation on heat transfer deterioration of supercritical pressure water in vertically-upward internally-ribbed tubes, *Int. J. Heat. Mass. Transf.* 120 (2018) 930–943, <https://doi.org/10.1016/j.ijheatmasstransfer.2017.12.097>.
- H.B. Li, M. Zhao, Z.X. Hu, Y. Zhang, F. Wang, Experimental study of supercritical water heat transfer deterioration in different channels, *Ann. Nucl. Energy* 119 (2018) 240–256, <https://doi.org/10.1016/j.anucene.2018.05.009>.
- M.F. Qu, D. Yang, Z.Y. Liang, L. Wan, D. Liu, Experimental and numerical investigation on heat transfer of ultra-supercritical water in vertical upward tube under uniform and non-uniform heating, *Int. J. Heat. Mass. Transf.* 127 (2018) 769–783, <https://doi.org/10.1016/j.ijheatmasstransfer.2018.08.079>.
- Z.X. Hu, D. Liu, H.Y. Gu, Study on spacer-induced heat transfer deterioration of supercritical water in annular channel, *Int. J. Heat. Mass. Transf.* 125 (2018) 552–558, <https://doi.org/10.1016/j.ijheatmasstransfer.2018.04.066>.
- G.A. Schatte, A. Kohlhepp, C. Wieland, H. Spliethoff, Development of a new empirical correlation for the prediction of the onset of the deterioration of heat transfer to supercritical water in vertical tubes, *Int. J. Heat. Mass. Transf.* 113 (2017) 1333–1341, <https://doi.org/10.1016/j.ijheatmasstransfer.2017.04.037>.
- G. Zhang, Y. Li, Y.J. Dai, Y.Z. Wang, Heat transfer to supercritical water in a vertical tube with concentrated incident solar heat flux on one side, *Int. J. Heat. Mass. Transf.* 95 (2016) 944–952, <https://doi.org/10.1016/j.ijheatmasstransfer.2016.01.011>.
- Z.H. Li, Y.X. Wu, J.F. Lu, D.L. Zhang, H. Zhang, Heat transfer to supercritical water in circular tubes with circumferentially non-uniform heating, *Appl. Therm. Eng.* 70 (2014) 190–200, <https://doi.org/10.1016/j.applthermaleng.2014.05.013>.
- G. Zhang, H. Zhang, H.Y. Gu, Y.H. Yang, X. Cheng, Experimental and numerical investigation of turbulent convective heat transfer deterioration of supercritical water in vertical tube, *Nucl. Eng. Des.* 248 (2012) 226–237, <https://doi.org/10.1016/j.nucengdes.2012.03.026>.
- S. Mokry, I. Pioro, A. Farah, K. King, S. Gupta, W. Peiman, et al., Development of supercritical water heat-transfer correlation for vertical bare tubes, *Nucl. Eng. Des.* 241 (2011) 1126–1136, <https://doi.org/10.1016/j.nucengdes.2010.06.012>.
- X. Cheng, Y.H. Yang, S.F. Huang, A simplified method for heat transfer prediction of supercritical fluids in circular tubes, *Ann. Nucl. Energy* 36 (2009) 1120–1128, <https://doi.org/10.1016/j.anucene.2009.04.016>.

- [16] J.F. Guo, M.R. Xiang, H.Y. Zhang, X.L. Huai, K.Y. Cheng, X.Y. Cui, Thermal-hydraulic characteristics of supercritical pressure CO₂ in vertical tubes under cooling and heating conditions, *Energy* 170 (2019) 1067–1081, <https://doi.org/10.1016/j.energy.2018.12.177>.
- [17] N. Kline, F. Feuerstein, F. Tavoularis, Onset of heat transfer deterioration in vertical pipe flows of CO₂ at supercritical pressures, *Int. J. Heat. Mass. Transf.* 118 (2018) 1056–1068, <https://doi.org/10.1016/j.ijheatmasstransfer.2017.11.039>.
- [18] Y.H. Fan, G.H. Tang, Numerical investigation on heat transfer of supercritical carbon dioxide in a vertical tube under circumferentially non-uniform heating, *Appl. Therm. Eng.* 138 (2018) 354–364, <https://doi.org/10.1016/j.applthermaleng.2018.04.060>.
- [19] M. Mohseni, M. Bazargan, A new analysis of heat transfer deterioration on basis of turbulent viscosity variations of supercritical fluids, *J. Heat. Transf.* 134 (2012) 122503–122507, <https://doi.org/10.1115/1.4007313>.
- [20] D. Huang, Wei Li, Heat transfer deterioration of aviation kerosene flowing in mini tubes at supercritical pressures, *Int. J. Heat. Mass. Transf.* 111 (2017) 266–278, <https://doi.org/10.1016/j.ijheatmasstransfer.2017.03.117>.
- [21] A. Urbano, F. Nasuti, Onset of heat transfer deterioration in supercritical methane flow channels, *J. Thermophys. Heat Transf.* 27 (2013) 298–307 <https://www.researchgate.net/publication/259496170>.
- [22] K. Yamagata, K. Nishikawa, S. Hasegawa, T. Fujii, S. Yoshida, Forced convective heat transfer to supercritical water flowing in tubes, *Int. J. Heat. Mass. Transf.* 15 (1972) 2575–2593, [https://doi.org/10.1016/0017-9310\(72\)90148-2](https://doi.org/10.1016/0017-9310(72)90148-2).
- [23] D. Huang, W. Li, A brief review on the buoyancy criteria for supercritical fluids, *Appl. Therm. Eng.* 131 (2018) 977–987, <https://doi.org/10.1016/j.applthermaleng.2017.12.042>.
- [24] D. Huang, Z. Wu, B. Sunden, W. Li, A brief review on convection heat transfer of fluids at supercritical pressures in tubes and the recent progress, *Appl. Energy* 162 (2016) 494–505, <https://doi.org/10.1016/j.apenergy.2015.10.080>.
- [25] G. Angelino, Carbon dioxide condensation cycles for power production, *J. Eng. Gas Turb. Power* 90 (3) (1968) 287–295, <https://doi.org/10.1115/1.3609190>.
- [26] K. Wang, M.J. Li, J.Q. Guo, P.W. Li, Z.B. Liu, A systematic comparison of different sCO₂ Brayton cycle layouts based on multi-objective optimization for applications in solar power tower plants, *Appl. Energy* 212 (2018) 109–121, <https://doi.org/10.1016/j.apenergy.2017.12.031>.
- [27] V. Dostal, A supercritical carbon dioxide cycle for next generation nuclear reactors, *Nuclear Engineering, Massachusetts Institute of Technology, 2004 PhD thesis*.
- [28] J.L. Xu, E.H. Sun, M.J. Li, H. Liu, B.G. Zhu, Key issues and solution strategies for supercritical carbon dioxide coal fired power plant, *Energy* 157 (2018) 227–246, <https://doi.org/10.1016/j.energy.2018.05.162>.
- [29] S.H. Liu, Y.P. Huang, G.X. Liu, J.F. Wang, L.K.H. Leung, Improvement of buoyancy and acceleration parameters for forced and mixed convective heat transfer to supercritical fluids flowing in vertical tubes, *Int. J. Heat. Mass. Transf.* 106 (2017) 1141–1156, <https://doi.org/10.1016/j.ijheatmasstransfer.2016.10.093>.
- [30] Z.H. Li, P.X. Jiang, C.R. Zhao, Y. Zhang, Experimental investigation of convection heat transfer of CO₂ at supercritical pressures in a vertical circular tube, *Exp. Therm. Fluid Sci.* 34 (2010) 1162–1171, <https://doi.org/10.1016/j.expthermflusci.2010.04.005>.
- [31] E.H. Sun, J.L. Xu, M.J. Li, G.L. Liu, B.G. Zhu, Connected-top-bottom-cycle to cascade utilize flue gas heat for supercritical carbon dioxide coal fired power plant, *Energy Convers. Manage.* 172 (2018) 138–154, <https://doi.org/10.1016/j.enconman.2018.07.017>.
- [32] Y.A. Cengel, M.A. Boles, *Thermodynamics—An Engineering Approach*, fifth ed., McGraw-Hill, New York, 1991, pp. 117–137.
- [33] M.I. Cabaco, M. Besnard, T. Tassaing, Y. Danten, Local density inhomogeneities detected by Raman scattering in supercritical hexafluorobenzene, *Pure. Appl. Chem.* 76 (2004) 141–146, <https://doi.org/10.1351/pac200476010141>.
- [34] K. Nishikawa, M. Takematsu, X-ray scattering study of carbon dioxide at supercritical states, *Chem Phys Lett.* 226 (1994) 359–363, [https://doi.org/10.1016/0009-2614\(94\)00728-4](https://doi.org/10.1016/0009-2614(94)00728-4).
- [35] G.G. Simeoni, T. Bryk, F.A. Gorelli, M. Krisch, G. Ruocco, M. Santoro, et al., The Widom line as the crossover between liquid-like and gas-like behaviour in supercritical fluids, *Nat. Phys. Lett.* 6 (2010) 503–507 <https://www.nature.com/articles/nphys1683>.
- [36] N. Metatla, F. Lafond, J.P. Jay-Gerin, A. Soldera, Heterogeneous character of supercritical water at 400 °C and different densities unveiled by simulation, *RSC Adv.* 00 (2012) 1–4, <https://doi.org/10.1039/C5RA25067F>.
- [37] A. Idrissi, I. Vyalov, Heterogeneity of the local structure in sub and supercritical ammonia: A Voronoi Polyhedra Analysis, *J. Phys. Chem. B* 115 (2011) 9646–9652, <https://doi.org/10.1021/jp204078u>.
- [38] J.L. Xu, T.K. Chen, A non-linear solution of inverse heat conduction problem for obtaining the inner heat transfer coefficient, *Heat Transf. Eng.* 19 (1998) 45–53, <https://doi.org/10.1080/01457639808939920>.
- [39] Z.H. Hu, *Heat transfer characteristics of vertical upflow and inclined tubes in the supercritical pressure and near-critical pressure region*, PhD thesis Thermal Power Engineering, Xi'an Jiaotong University, 2001.
- [40] D.T. Banuti, Crossing the Widom-line – Supercritical pseudo-boiling, *J. Supercrit. Fluid* 98 (2015) 12–16, <https://doi.org/10.1016/j.supflu.2014.12.019>.
- [41] J.W. Ackerman, Pseudo-boiling heat transfer to supercritical pressure water in smooth and ribbed tubes, *J. Heat. Transf.* 92 (3) (1970) 490–497, <https://doi.org/10.1115/1.3449698>.
- [42] D.T. Banuti, *Thermodynamic analysis and numerical modeling of supercritical injection*, Ph.D. thesis Institute of Aerospace Thermodynamics University of Stuttgart, 2015.
- [43] S.G. Kandlikar, Heat transfer mechanisms during flow boiling in micro channels, *J. Heat Transf.* 126 (2004) 8–16, <https://doi.org/10.1115/1.1643090>.
- [44] Y.Y. Bae, H.Y. Kim, D.J. Kang, Forced and mixed convection heat transfer to supercritical CO₂ vertically flowing in a uniformly-heated circular tube, *Exp. Therm. Fluid Sci.* 34 (2010) 1295–1308, <https://doi.org/10.1016/j.expthermflusci.2010.06.001>.
- [45] D.E. Kim, M.H. Kim, Experimental investigation of heat transfer in vertical upward and downward supercritical CO₂ flow in a circular tube, *Int. J. Heat Fluid Fl.* 32 (2011) 176–191, <https://doi.org/10.1016/j.ijheatfluidflow.2010.09.001>.
- [46] K. Jiang, *An experimental facility for studying heat transfer in supercritical fluids*, PhD thesis Mechanical Engineering, Ottawa-Carleton Institute for Mechanical and Aerospace Engineering, 2015.
- [47] J.D. Jackson, W.B. Hall, Influences of buoyancy on heat transfer to fluids flowing in vertical tubes under turbulent conditions, *Turbulent Forced Convection in Channels and Bundles, Hemisphere*, 2 1979, pp. 613–640.
- [48] J.D. Jackson, Fluid flow and convective heat transfer to fluids at supercritical pressure, *Nucl. Eng. Des.* 264 (2013) 24–40, <https://doi.org/10.1016/j.nucengdes.2012.09.040>.
- [49] S. Yildiz, D.C. Groeneveld, Diameter effect on supercritical heat transfer, *Int. Commun. Heat. Mass.* 54 (2014) 27–32, <https://doi.org/10.1016/j.icheatmasstransfer.2014.02.017>.